THREE-DIMENSIONAL PRANDTL-TOMLINSON MODEL OF NANOSCALE FRICTION

by

© Mafruha Akhter Ovi

A Thesis submitted to the Department of Physics and Physical Oceanography in partial fulfillment of the requirements for the degree of Master of Science

Department of Physics and Physical Oceanography

Memorial University of Newfoundland

May 2019

St. John's Newfoundland and Labrador

Abstract

Friction is a complex phenomenon that involves interaction between microsized asperities on the surfaces of two bodies in contact. Friction force microscopy allows investigating friction forces that arise at the level of a single asperity, which is the tip of an atomic force microscope (AFM). In this thesis, the Prandtl-Tomlinson model of single-asperity friction is developed that fully incorporates the three-dimensional character of the problem. An algorithm is derived that allows integrating the resulting equations of motion. Special care is taken to select the model parameters close to the values that can be deduced from the experimental results published in the literature. The effect of periodic actuation of the AFM cantilever on the resulting friction forces is studied within this model. Three actuation modes are considered: transverse, normal, and lateral. Transverse actuation has no effect whatsoever on the friction force, whereas the effect of normal actuation is somewhat weaker than the effect of lateral actuation. Due to the finite mass of the cantilever, its motion may proceed in many different regimes which depend on the actuation amplitude and frequency. Hence, the dependence of friction force on actuation frequency at fixed amplitude and on the actuation amplitude at fixed frequency is obtained numerically. Both dependences are not simple and consist of a series of irregular peaks. Those peaks are more pronounced at zero temperature than at room temperature. Finally, the limitations of the model are discussed. It is suggested that two effects must be incorporated into the model in order to provide a more realistic picture of the nanoscale friction: the finite elasticity of the apex of the cantilever tip and the aging of the tip-sample contact.

Acknowledgment

I would like to express my sincere gratitude to my supervisor Dr. Mykhaylo Evstigneev for the continuous support of my Masters Study and research, for his patience, motivation, enthusiasm, and immense knowledge. His guidance helped me in all the time of research and writing of this thesis.

My heartiest gratitude to my husband for time and mental support he gave me throughout the study period. I also thank my family back home for their support and well wishes.

Thanks to those of my wonderful classmates and friends who always supported me with positive motivations.

Contents

List of tables

List of figures

Chapter I

Introduction

1.1 Historical background

If relative motion of bodies is part of a process, friction is a necessary component of it, no matter if the surfaces involved are the surface of an ocean and a ship or a violin bow and a string. It is not an exaggeration to say that friction is essential in our everyday life. It would be impossible to ride a bicycle, drive a car, or even walk without friction. Many industrial activities crucially depend on friction, both in a positive or negative ways.

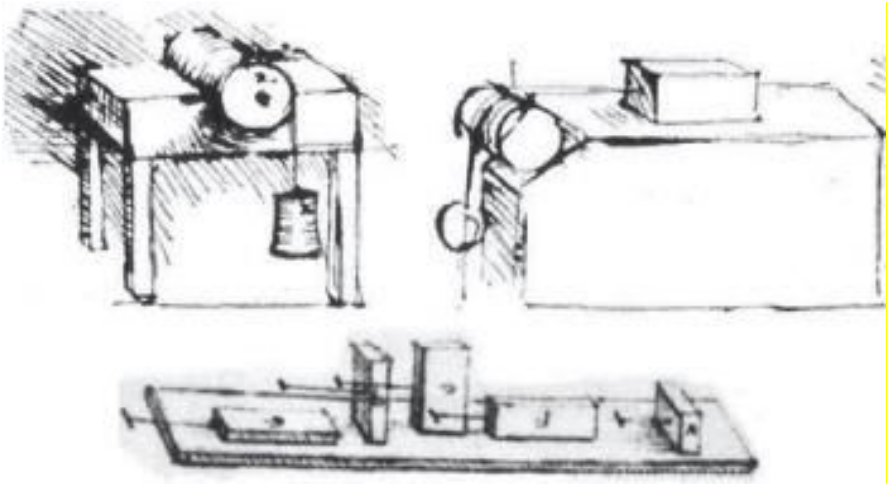

Figure1.1: Sketches from da Vinci's notebook, ca. 1480, demonstrating some of his notable friction experiments [Pit14].

Tribology is a science of friction. The first documentation in tribology was produced by Leonardo da Vinci in the late 15th century. Some sketches from his notebook, shown in Figure1.1, give an idea how he measured friction between two objects. Da Vinci's original statements are:

1. The friction made by blocks of the same weight is independent of the contact area.
2. Friction produces double the amount of effort if the weight be doubled.

These two statements would later become the first two laws of friction, attributed to Guillaume Amontons.

Da Vinci did his experiment about two centuries prior to the introduction of the concept of force by Isaac Newton in his Principia in 1678. After Newton's ground-breaking work, Charles Coulomb performed a more quantitative research on sliding friction. He systematically investigated the effect of different factors, such as the nature of the materials in contact, the normal pressure, the size of the surface of contact and the ambient conditions. He summarized many of his results in the statement that friction is proportional to load and that the coefficient of proportionality, the friction coefficient, is usually almost independent of the load, the sliding velocity, and the area of contact. He also made a distinction between the static and kinetic friction coefficients, which are the

proportionality coefficients between the normal load and the minimal force necessary to initiate motion (static friction) and to maintain motion (kinetic friction).

The microscopic foundations of these laws started to be uncovered only in the middle of the 20th century. These studies were initiated by the works of Bowden and Tabor, who summarized their results in the classic textbook, which was originally published in 1950 and is of importance even today [Bow01].

The basic idea behind the Bowden-Tabor theory is that the contact between two apparently flat surfaces actually consists of many point-like contacts formed by microsized asperities. Hence, one should distinguish between the apparent contact area, A, and the real contact area, A_{real}, which is many orders of magnitude smaller than A. For simplicity, let us consider the friction force that arises when two pieces of the same material are pressed against each other. In contrast to the fixed apparent contact area, the real contact area is proportional to the normal load as $\sigma A_{real} = F_N$, where the parameter σ is called the penetration hardness of the material. The physical meaning behind this relation is simple: as two surfaces are pressed against each other, the contact asperities deform, thereby increasingA_{real}, until they are able to support the normal load. At the points of contact, the asperities belonging to the opposite surfaces form cold-welded junctions. In order to start motion, one needs to break those junctions by applying a shearing force. This force is proportional to the total junction area, A_{real}, with the proportionality constant being the yield stress against shear, denoted as τ. Thus, static friction $F_S = \tau A_{real} = \tau F_N/\sigma = \mu_S F_N$ is proportional to normal load and independent of the apparent contact area. The static friction coefficient is given by the ratio $\mu_S = \tau/\sigma$, which turns out to be in reasonably good agreement with the experiment.

This simple reasoning explains a lot about static friction. However, it does not give the complete picture of friction, as the following argument due to Archard [Arc57] demonstrates. Let us consider what happens at the contact between two asperities. We may view the two asperities as spheres. It follows from the contact theory by Hertz,

developed in 1880's and reviewed, e.g., in Chapter 15.5 of [Isr11], that when two spheres are pressed against each other by a force F, then the radius of their contact region will scale as $F^{1/3}$, and the contact area will scale, therefore, as $F^{2/3}$. If we combine this observation with Bowden-Tabor theory, we would have to conclude that the static friction force should increase as $F_N^{2/3}$, in disagreement with the Amonton's law. The way out of this difficulty is to take into account that not only the real contact area, but also the number of microscopic contacts increases with the normal load

At present, there is no fundamental theory that covers friction both in the macro and nanoscale. One of the reasons why friction is such a complex phenomenon is because it involves processes on many different length scales, from the macroscopic lengths of centimeters, to the micrometer size of the asperities, to the nanometer size of the contact between asperities, down to the size of single atoms. Due to the development of instrumentation and computational tools, it is now possible to better understand the fundamental mechanisms of friction, as we can observe microscale asperities with these techniques.

1.2 Basic experimental approaches

There are three instruments that play key role in nanometer scale friction experiments that will be presented shortly here.

1.2.1 Atomic force microscope (AFM)/friction force microscope (FFM)

The Atomic force microscope (AFM) was invented by Gerd Binnig et al in 1986 [Bin86] and applied to study nanofriction a year later by Mate et al [Mat87]. Tribological application of AFM is usually referred to as friction force microscopy (FFM). A schematic illustration of an AFM/FFM experiment is shown in Figure 1.2. An FFM has an atomically sharp tip that is brought in contact with the surface of a material and scanned over it. As a result of interactions between the cantilever tip and the surface, the cantilever beam will twist from equilibrium. This deflection can be measured optically.

The resulting instantaneous friction force can be deduced from the knowledge of the cantilever is elastic properties. In this way, FFM is focused on the friction studies at a single-asperity level and will be of main interest in this thesis.

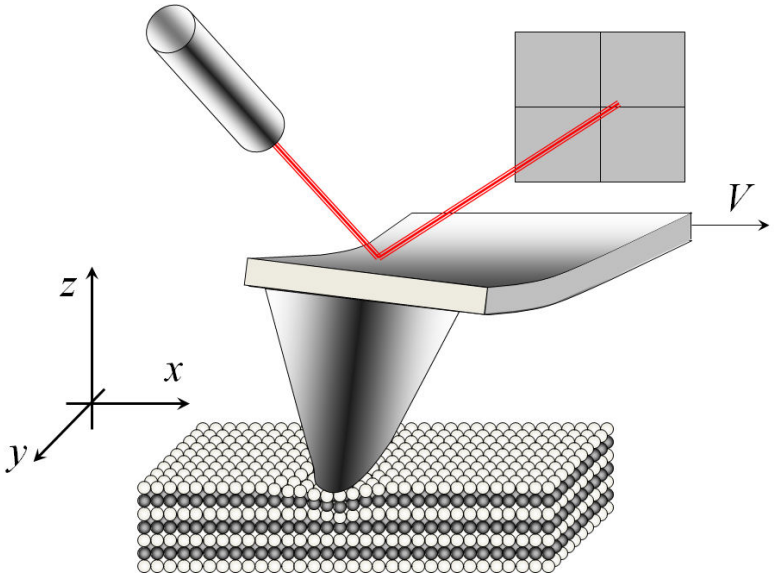

Figure1.2: Schematics of an atomic force microscope used for nanofriction measurements.

The typical length of the cantilever tip is in the micrometer range, and the typical radius of curvature of its apex, R_{apex}, is of the order of 10 nm. Even though the tip is sometimes referred to as "atomically sharp", the tip-substrate contact actually consists of many atoms, as the following estimate shows. Let us define the contact atoms as those atoms on the tip apex that are closer to the surface than a few lattice constant, say, within the distance d = 1 nm. Note that $R_{apex} \gg d$. Then, the lower bound for the contact area can be found from elementary geometry and/or dimensional analysis to be $A_{contact} \sim R_{apex} d$, and the number of contact atoms is estimated to be $N_{contact} \sim \frac{A_{contact}}{a^2}$. Assuming R_{apex} = 10 nm and the lattice constant a = 0.3 nm, we obtain conservative estimates $A_{contact} \sim 10$ nm^2 and $N_{contact} \sim 100$. The tip-substrate contact is formed by a few hundred atoms.

1.2.2 Quartz crystal microbalance (QCM)

The quartz crystal microbalance (QCM) technique employs the sensitivity of a quartz crystal oscillation frequency and quality factor to the atoms that are absorbed on its surface. This technique has been first adapted for nanofriction studies by Jacqueline Krim et al in 1991 [Kri91]. It measures the friction force at the level of single atoms. Interestingly, the results of these measurements indicate that friction force acting between single atoms is proportional to their velocity, $F \sim v$ [Kri13], in sharp contrast to Coulomb law for velocity-independent macroscopic friction. This linear dependence of the dissipative force between an atom and the surface follows directly from the linear-response theoretic arguments [Evs10, Evs19].

1.2.3 Surface force apparatus (SFA)

The surface force apparatus was invented by David Tabor and R.H.S. Winterton in 1969 [Tab69]. At the heart of a surface force apparatus are two crossed cylinders, usually made of mica, in contact with each other [Tia13]. The cylinders are pressed against each other by adhesion and an external load. They can be set in relative motion by means of a piezo element, and the resulting friction force can be measured. The radius of curvature of the cylinders ranges between a few millimeters to a few centimeters. Then, employing the estimate from Section 2.1 for the contact area, we obtain, assuming the cylinder radius R = 1 mm and taking the same parameters d = 1 nm, a = 0.3 nm as in Section 2.1: $A_{contact} \sim 10^6$ nm^2 and $N_{contact} \sim 10^7$. This is five orders of magnitude higher than the AFM contact area.

3. Structure of this thesis

In this work, we focus on FFM nanofriction from Section 1.2.1. The standard theoretical model to describe these experiments is the one-dimensional Prandtl-Tomlinson model [Rie03, Evs13]. As the name suggests, it does not take into consideration the full three-dimensional character of the experiment, see Figure 1.2. Relatively recently, a three-dimensional extension of this model has been made in [Wie11], but as will be explained

later in the end of Chapter II, the model from [Wie11] works only when the tip is in contact with the substrate. Our main goal is to generalize the model to be able to treat arbitrary distances between the tip and the substrate, and to apply it to study the effect of cantilever actuation on friction forces.

In this thesis, a three-dimensional model of FFM single-asperity friction is developed in Chapter II. In Chapter III, a numerical algorithm is derived that allows integrating the equations of motion of this model. Chapter IV is central in this thesis, as it presents the numerical results that relate the friction force to the experimental control parameters, such as pulling velocity, temperature, and actuation of the cantilever base. Finally, Chapter V summarizes our findings and also briefly discusses the limitations of our model, which should be taken into account in order to get a more realistic picture of nanoscale friction.

Chapter II

Prandtl-Tomlinson model

2.1 One-dimensional Prandtl-Tomlinson (1dPT) model

2.1.1 Stick-slip process

The Prandtl-Tomlinson (PT) model is one of the most commonly used models in nanoscale friction. It was originally introduced by Ludwig Prandtl [Pra28] (see an overview and an English translation of Prandtl's original paper from German in [Pop12]) and George Tomlinson [Tom29]. In spite of its simplicity, the model captures all features of the stick-slip process generally observed in AFM friction experiments, in which the AFM tip is dragged along an atomically flat surface. In the stick-slip regime, the force of

friction, deduced from the elastic deformation of the cantilever, changes in time in a saw tooth-like manner see Figure 2.1. The process consists of the following phases:

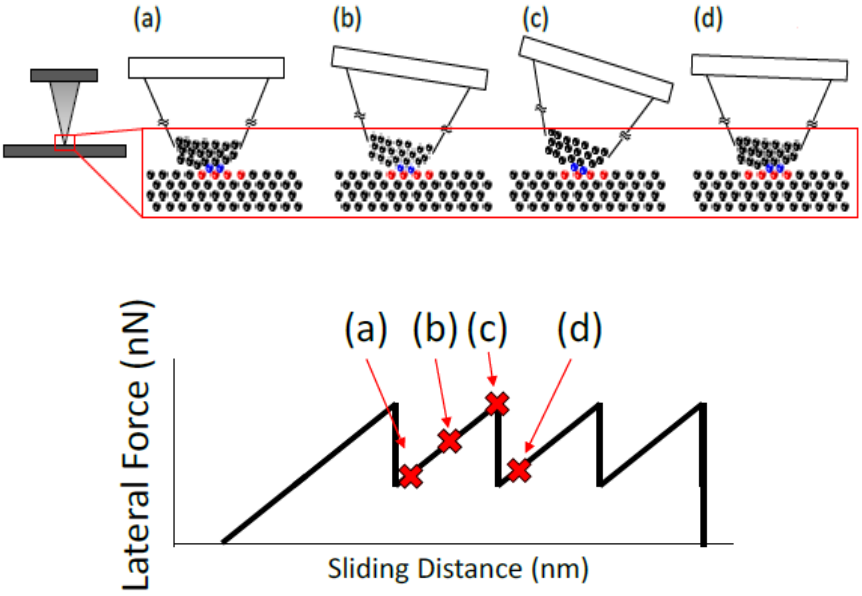

Figure 2.1: Stick-slip motion for an AFM tip

(a) Initially, the tip finds itself in one of the lattice sites of the surface.

(b) As the cantilever base moves, the elastic deformation of the cantilever increases, leading to a reduction of the potential barrier that separates the tip from the next minimum.

(c) This barrier disappears when the elastic force in the cantilever becomes equal to the maximal force produced by the surface potential.

(d) After overcoming the static friction threshold, the asperity jumps into the next potential minimum, at the same time dissipating its kinetic energy into the phonon and electron subsystems of the substrate. Eventually, the tip settles down to the next lattice site, and the process repeats itself.

2.1.2 Time scales

It is clear from the beginning that the system, schematically depicted in Figure 2.1 and in Figure 2.2, is characterized by several groups of the degrees of freedom, and that each group has its own characteristic time scale. These groups are listed in this section in the order from the slowest to the fastest.

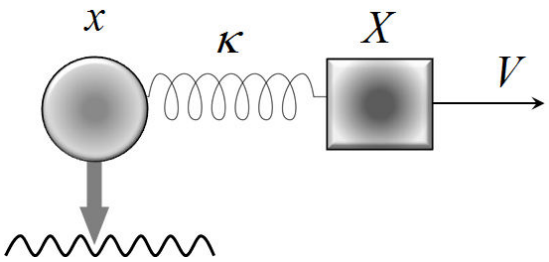

Figure 2.2: Schematic representation of an AFM friction experiment from Figure 1. The square block represents cantilever base, the ball corresponds to the tip, and the arrow to the tip apex.

Cantilever base. The slowest time scale is associated with the motion of the cantilever base, which moves with the velocity V of the order of a few microns per second. Hence, the time needed for the base to cover the distance of one lattice constant is in the millisecond range.

Torsional cantilever deformation. In nanofriction experiments, the measured quantity is the torsional deformation of the cantilever beam (see Figure 2.2). The typical torsional oscillation frequency is of the order of a few hundred kHz, implying the respective time scale to be in the microsecond range.

Tip apex consists of at most a few hundred thousand atoms and is many orders of magnitude smaller than the rest of the cantilever [Rei04]. According to the estimate from [Kry06, Kry07], the respective time-scale associated with the tip apex oscillations is in the nanosecond range.

Atomic degrees of freedom. Finally, the time-scale that characterizes the motion of single atoms is of the order of inverse Debye frequency and is in the femto- to picosecond range.

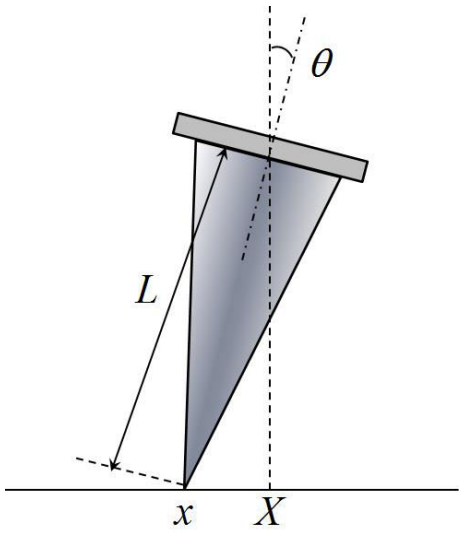

Figure 2.3: The relevant coordinates in the 1dimensinal Prandtl-Tomlinson (1dPT) model.

In view of this huge time-scale separation, and because of a very large number of atoms involved, direct molecular dynamics simulation of the problem is severely limited with respect to the size of the system and the time-scales that can be probed. Hence, we will develop a stochastic model, which involves only the slow variables: the position of the cantilever base and the torsional deformation of the tip. The fast degrees of freedom describing the tip apex deformation and possibly other fast deformation modes of the cantilever, as well as the atomic degrees of freedom are taken into account implicitly in the form of an effective potential, dissipation, and noise [San01, Rei04, Rei05].

Thus, we have two slow variables in the 1dPT model (see Figure 2.3 showing the cantilever side view):

- The cantilever base, whose coordinate is given by

$$X = Vt; \tag{2.1}$$

- The torsional deformation of the cantilever. In principle, it is possible to parametrize the torsional deformation by the corresponding deformation angle, θ, see Figure 2.3 However, it is more convenient to adopt an equivalent picture, in which it is characterized by the position x defined as

  $$X - x = L \sin\theta \approx L\theta \,, \tag{2.2}$$

  where L is the tip length. We have set $\sin\theta \approx \theta$. It is an excellent approximation, because the typical length of an AFM tip is in the micrometer range, and the typical value of $|X - x|$ is in the nanometer range, i.e. $\sin\theta \sim 10^{-3}$. The geometric meaning of the coordinate x is the position that the tip apex would have if the tip were absolutely rigid, i.e. in the absence of its elastic deformation, see Figure 2.3 The actual position of the tip apex differs from x by a small amount. In the following, we will refer to the coordinate x as "the tip coordinate" keeping this difference in mind.

The remaining atomic degrees of freedom, as well as the deviation of the tip apex from the position x from the last equation, and possibly other deformation modes of the cantilever are so fast that, at each moment of time, they can be considered to be almost in thermal equilibrium state at given values of x and X.

2.1.3 Energy considerations

2.1.3.1. Elastic energy

The elastic energy stored in the cantilever is proportional to the deviation squared of the tip position from the mechanical equilibrium position, which we set equal to the position X of the cantilever base without loss of generality:

$$U_{el}(X - x) = \frac{\kappa(X-x)^2}{2} \,. \tag{2.3}$$

Here, the effective spring constant κ describes the combined effect of the elastically deformed cantilever spring, the tip, and the surface in the contact region. Because the "springs" associated with each such deformation are connected in series, the effective

spring constant measured experimentally is given by [Lan97a, Lan97b, Col96, Car97, Joh98, Ben99]

$$\frac{1}{\kappa} = \frac{1}{\kappa_{cantilever}} + \frac{1}{\kappa_{tip}} + \frac{1}{\kappa_{surface}} . \tag{2.4}$$

The instantaneous force of friction is equal to the elastic force generated by the spring:

$$f = -\kappa(x - X) . \tag{2.5}$$

Hence, the effective stiffness can be determined from the slope $\kappa = \frac{df}{dX}$ of the force-distance curve in any stick phase, when the tip position x is approximately constant.

2.1.3.2 Surface potential

The periodically arranged atoms of the surface create an additional potential, which is periodic in the relevant coordinate x. This potential is usually modeled with a trigonometric function of periodicity a and the corrugation depth U_0 [San01]:

$$U_S(x) = -\frac{U_0}{2}\cos\frac{2\pi x}{a} . \tag{2.6}$$

In mechanical equilibrium, the position of the tip at a given time t is determined by setting the first derivative of

$$U(x, X) = U_S(x) + U_{el}(X - x) \tag{2.7}$$

with respect to x,

$$\frac{\partial U(x,t)}{\partial x} = \frac{\pi U_0}{a}\sin\frac{2\pi x}{a} + \kappa(x - X) \tag{2.8}$$

to zero. In order for this equation to have more than one solution, the maximal curvature of the surface potential must be greater than the effective stiffness κ. The maximal value of the second derivative of the substrate potential is

$$\max_x \frac{d^2 U_S}{dx^2} = \frac{2\pi^2 U_0}{a^2} , \tag{2.9}$$

and thus the stick-slip instability occurs only when the so-called Prandtl-Tomlinson parameter [Soc04, Med06] exceeds 1,

$$\gamma_{PT} = \frac{2\pi^2 U_0}{\kappa a^2} > 1 . \tag{2.10}$$

Otherwise, the total potential of the tip is monostable, making steady sliding the only possible regime of motion.

The tip becomes unstable and gets ready to move to the next minimum when the second derivative of the total potential vanishes, $\frac{\partial^2 U_{tot}}{\partial x^2} = 0$, giving the critical tip position

$$x_c = \frac{a}{2\pi}\cos^{-1}(\gamma_{PT}^{-1}) \,. \tag{2.11}$$

As a result of a slip, the elastic energy is transformed into the tip's kinetic energy, which gets dissipated into thermal energy, involving the irreversible process of friction.

Depending on the value of γ_{PT}, the total potential may have one, two, three, etc. minima, with the number of minima increasing with increasing γ_{PT}. In a multistable potential, the tip may jump over a multiple number of lattice spacing [Nak05]. Multiple jumps have been observed experimentally [Mat87, Med06, Rot10] and were interpreted as an indication of the tip inertia effect. An alternative interpretation [Evs13] suggests that these multiple jumps are actually very short-lived stick phases, whose duration is shorter than the experimental temporal resolution.

2.1.4 Inertia, dissipation, and noise

In order to describe energy dissipation during the slip events, we should complement the model by including the inertia and dissipative terms in the cantilever equation of motion. In the inertial term, $m\ddot{x}$, the effective mass parameter m is associated with the torsional deformations of the tip. The dissipative force can be described as a viscous force, which is proportional to the tip's velocity relative to the surface, with the proportionality constant being the surface damping coefficient:

$$f_S^{diss} = -\eta_S \dot{x} \,. \tag{2.12}$$

The minus sign implies that the force is directed against the velocity, ultimately leading to the tip's slowing down.

The tip's relative motion with respect to the cantilever base leads to an additional energy dissipation mechanism, with the respective dissipative force being proportional to the velocity of the tip relative to the cantilever base [Rei04, Rei05]:

$$f_C^{diss} = -\eta_C(\dot{x} - V) \tag{2.13}$$

with the proportionality coefficient η_C being the cantilever damping constant.

The last two forces are sometimes referred to as "viscous friction" in view of their formal analogy with viscous friction in liquids, but this analogy is actually poor [Kry14]. Rather, the reason for the linear relation between the damping force and the tip velocity $\dot{x}$ can be found in linear response arguments [Evs10, Evs19].

In addition to dissipation, the irrelevant fast degrees of freedom produce a random force $\xi(t)$, or noise, that affects the cantilever's dynamics. This random force has zero mean value:

$$\langle \xi(t) \rangle = 0 \ . \tag{2.14}$$

Because the dynamics of the irrelevant degrees of freedom is many orders of magnitude faster than the tip's dynamics, we can set the autocorrelation time of this noise to zero and approximate its autocorrelation with Dirac delta function. Hence, the noise autocorrelation function is

$$\langle \xi(t)\xi(t') \rangle = 2(\eta_C + \eta_S)k_B T\delta(t - t') \ . \tag{2.15}$$

Here, $k_B T$ is the thermal energy. The factor in front of the delta function is uniquely determined by the fluctuation-dissipation theorem of the second kind [Kub66]. Basically, the noise autocorrelation function is of the form (2.15) in order to ensure that the tip's equilibrium probability distribution becomes equation of Maxwell-Boltzmann type in the absence of pulling [Evs10].

Collecting all forces together, we write the Langevin equation for the tip:

$$m\ddot{x} = -\frac{dU}{dx} - \eta_S\dot{x} - \eta_C(x - V) - \kappa(x - X) + \xi(\mathrm{t}) \ . \tag{2.16}$$

The 1dPT model has been studied extensively in a number of publications [San01, Rie03, Rei04, Rei05, Nak05, Med06, Tsh09, Evs13]. Various extensions of this basic model exist to include the possibility of multiple contacts [Mai05], tip lateral motion in the direction perpendicular to the pulling velocity [Ste09, Rot10], or in the normal direction [Tsh05, Hol08]. A three-dimensional treatment is presented in [Wie11].

2.2 Three-dimensional Prandtl-Tomlinson (3dPT) model

2.2.1 Equations of motion

Here, we generalize the model of [Wie11] to incorporate the effects that are overlooked by it. As before, we consider the cantilever torsional deformation as the slow coordinate described by the position $\vec{r} = (x, y, z)$ that the tip apex would have if the tip were absolutely rigid. We denote as $\vec{R} = (X, Y, Z)$ that position of the cantilever tip at which the elastic energy is minimal. Because it is completely determined by the location of the cantilever base, we will refer to $\vec{R}$ as "the cantilever base position", keeping in mind that the actual location of the cantilever base is offset from $\vec{R}$ in the vertical direction by the length of the cantilever tip.

The motion of the tip in the normal z- or the lateral x- or y-direction is associated with different deformation patterns of the cantilever. To each deformation pattern corresponds its own portion of the cantilever that is actually moving. Furthermore, an external force applied to the tip in, say, the x-direction may, in principle, result in its acceleration in the y- or z-direction. Hence, the cantilever mass should be a tensor $\boldsymbol{m}$. It must be positive definite, because the kinetic energy $\frac{1}{2}\vec{v}^T\boldsymbol{m}\vec{v}$ of the tip is positive.

Next, the motion of the tip in, say, x-direction may result in an onset of the dissipative force in the y- or z-direction. Hence, the damping coefficient of the cantilever and the substrate should become tensors $\boldsymbol{\eta}_S$ and $\boldsymbol{\eta}_C$. Because the power produced by the

dissipative force is negative, we must have $\vec{v}^T \boldsymbol{\eta}_{C,S} \vec{v} > 0$ for any velocity $\vec{v}$, i.e. the dissipation tensors must be positive definite.

Finally, the elastic coefficient $\boldsymbol{\kappa}$ should become a tensor as well. It must be positive definite, because the elastic energy $\frac{1}{2}\left(\vec{r} - \vec{R}\right)^T \boldsymbol{\kappa}\left(\vec{r} - \vec{R}\right) > 0$ for all deformations $\vec{r} - \vec{R}$.

The equations of motion of the tip read in the most general form:

$$\boldsymbol{m}\ddot{\vec{r}} = -\frac{\partial U}{\partial \vec{r}} - \boldsymbol{\kappa}\left(\vec{r} - \vec{R}\right) - \boldsymbol{\eta}_S \dot{\vec{r}} - \boldsymbol{\eta}_C \left(\dot{\vec{r}} - \dot{\vec{R}}\right) + \vec{\xi}(\vec{r}, t) \ . \tag{2.17}$$

Due to the fluctuation-dissipation theorem of the second kind, the noise correlation function is

$$\langle \vec{\xi}(\vec{r}, t) \vec{\xi}^T(\vec{r}', t') \rangle = 2k_B T \, \boldsymbol{\eta} \, \delta(t - t') \ , \ \boldsymbol{\eta} = \ \boldsymbol{\eta}_S + \boldsymbol{\eta}_C \ , \tag{2.18}$$

where the superscript *T* indicates transposition.

2.2.2 Elastic energy and substrate potential

2.2.2.1. Elastic energy

The elastic energy stored in the cantilever is given by a quadratic form

$$U_{el}\left(\vec{r}, \vec{R}\right) = \frac{1}{2}(\vec{r} - \vec{R})^T \boldsymbol{\kappa}(\vec{r} - \vec{R}) \ . \tag{2.19}$$

Here, the superscript T means vector transposition, and $\boldsymbol{\kappa}$ is a 3×3 matrix of elastic constants. To keep things simple, we assume that it is diagonal with the coefficients $\kappa_{xx} = \kappa_{yy} = \kappa_L$ being the lateral stiffness and $\kappa_{zz} = \kappa_N$ being the normal stiffness:

$$\boldsymbol{\kappa} = \begin{pmatrix} \kappa_L & 0 & 0 \\ 0 & \kappa_L & 0 \\ 0 & 0 & \kappa_N \end{pmatrix}. \tag{2.20}$$

The lateral friction force is then given by the projection of the elastic force on the direction of pulling:

$$f_L(t) = -\frac{\vec{V}^T \boldsymbol{\kappa}(\vec{r} - \vec{V}t)}{|\vec{V}|} \, , \tag{2.21}$$

where the pulling velocity $\vec{V}$ has zero z-component, as pulling proceeds in the xy-plane. The friction force is found as the time average

$$< f_L >= \lim_{t\to\infty} \frac{1}{t}\int_0^\infty dt' f_L(t') \tag{2.22}$$

And the normal load is found as the mean value

$$f_N = \kappa_N\langle(z - Z)\rangle = \lim_{t\to\infty} \frac{\kappa_N}{t}\int_0^\infty dt'(z(t') - Z) \, . \tag{2.23}$$

2.2.2.2. Substrate potential

The potential of interaction between the tip and the substrate must be periodic in the lateral coordinates x and y. Hence, it can be decomposed into a Fourier series with the Fourier coefficients depending on the normal coordinate z. We assume the following functional form of this potential:

$$U_S(x, y, z) = U_0(z) + U_1(z)\psi(x, y) \, . \tag{2.24}$$

Here, $U_0(z)$ is the tip-substrate interaction energy averaged with respect to the lateral coordinates x and y.

Assuming for simplicity that the substrate potential is periodic in x and y with the same periodicity a, the "egg-filler function" $\psi(x, y)$ is such that

$$\psi(x + la, y + ka) = \psi(x, y) \, , \tag{2.25}$$

with integer l and k. Without loss of generality, we impose the requirement that

$$\begin{aligned} &\psi(x, y) = 0 \text{ whenever } (x, y) = (la, ka) \, ; \\ &\psi(x, y) = 1 \text{ whenever } (x, y) = ((l + 1/2)a, (k + 1/2)a) \, . \end{aligned} \tag{2.26}$$

We assume that

$$\psi(x, y) = \frac{1}{2} - \frac{1}{4}\left(\cos\left(\frac{2\pi x}{a}\right) + \cos\left(\frac{2\pi y}{a}\right)\right) \, . \tag{2.27}$$

A sample plot of the egg-filler function is shown in Figure 2.4

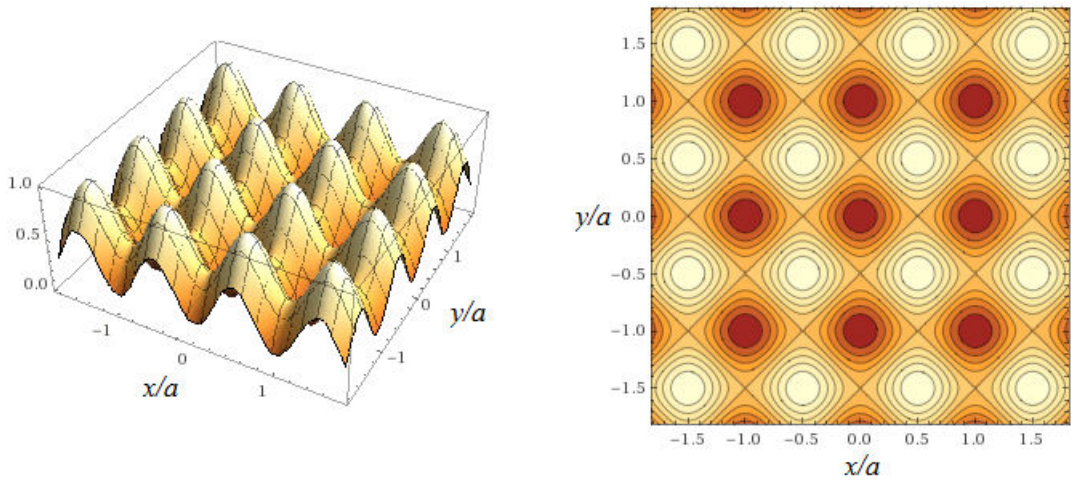

Figure 2.4: The 3d (left) and contour plot (right) representation of the egg-filler function $\psi(x, y)$ from Eq. (11).

Returning to the first term, $U_0(z)$, in Eq. (2.24), it must have an attractive and a repulsive part. The attractive contribution arises due to the van der Waals interaction between the tip and the semi-infinite substrate. After integrating the van der Waals potential $U_{vdW} \propto -1/r^6$ over the tip and the substrate volume, the result is that $U_0(z) \propto -\frac{1}{z}$ at large distances [Arg96].

At short distances, the potential $U_0(z)$ must be repulsive because of the elastic deformation of the substrate and the cantilever tip apex. The exact functional form of the repulsive part of the potential energy is unknown, so we choose it at short distances to decay with z as $1/z^\beta$ with the exponent $\beta > 1$. Combining the two asymptotic forms, we obtain the potential of Mie type with the equilibrium separation σ and the potential depth ε:

$$U_0(z) = \frac{\varepsilon}{\beta - 1}\left[\left(\frac{\sigma}{z}\right)^\beta - \beta\frac{\sigma}{z}\right]. \tag{2.28}$$

It is shown in Figure 2.5

Keeping in mind that corrugation of the potential $U(x, y, z)$ stems from the same origin as its repulsive part, namely, interaction between the tip and the substrate atoms in its immediate vicinity, we choose the same functional form for the corrugation depth $U_1(z)$ as the repulsive part of $U_0(z)$, namely

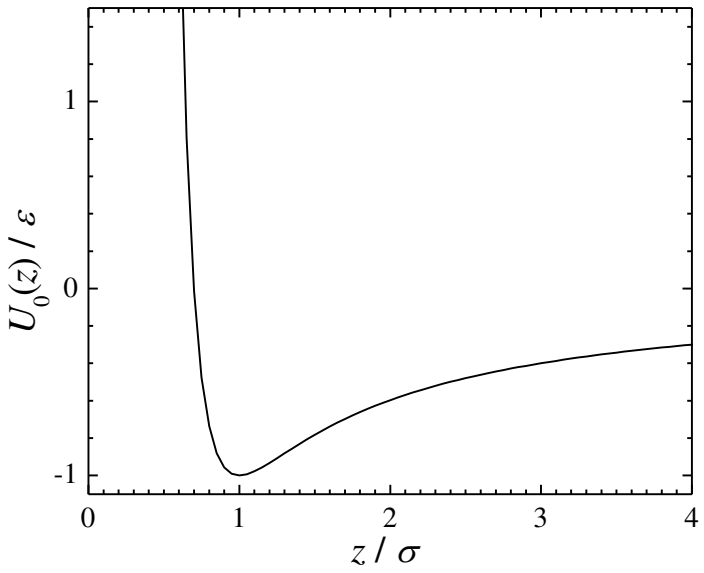

Figure 2.5: The Mie potential used to model the uncorrugated part of the tip-surface interaction $U_0(z)$ with $\beta = 6$.

$$U_1(z) = -h\frac{\varepsilon}{\beta-1}\left(\frac{\sigma}{z}\right)^{\beta} . \tag{2.29}$$

The magnitude of the corrugation parameter h cannot exceed 1, because otherwise the total potential

$$U(\vec{r}) = \frac{\varepsilon}{\beta-1}\left[\left(1 - h\left[\frac{1}{2} - \frac{1}{4}\left(\cos\left(\frac{2\pi x}{a}\right) + \cos\left(\frac{2\pi y}{a}\right)\right)\right]\right)\left(\frac{\sigma}{z}\right)^{\beta} - \beta\frac{\sigma}{z}\right] \tag{2.30}$$

will diverge to $-\infty$ rather than to $+\infty$ as $z \to 0$ at lateral coordinates (x, y) equal to integer multiples of a.

2.2.3 Dissipative force and mass

To keep the number of parameters minimal, we take the mass tensor in Eq. (2.17) to be diagonal:

$$\boldsymbol{m} = m\boldsymbol{I}\,. \tag{2.31}$$

As in the 1dPT case, the dissipative force on the tip has two contributions: one arises due to the cantilever degrees of freedom and is proportional to the tip velocity relative to the cantilever base, and the other stems from the substrate atoms in contact with the tip apex and is proportional to the tip velocity relative to the substrate.

Because we now allow for the three-dimensional motion of the tip, the cantilever damping force depends on all velocity components and is written, in the most general form, as

$$\vec{f}_C^{diss} = -\boldsymbol{\eta}_C\left(\dot{\vec{r}} - \dot{\vec{R}}\right), \tag{2.31}$$

where $\boldsymbol{\eta}_C$ is the dissipation coefficient matrix of the cantilever. Similarly, the degrees of freedom of the substrate give rise to the dissipative force

$$\vec{f}_C^{diss} = -\boldsymbol{\eta}_S\dot{\vec{r}}\,. \tag{2.32}$$

For the sake of simplicity, we assume both dissipation tensors to be diagonal:

$$\boldsymbol{\eta}_C = \eta_C\boldsymbol{I}\,,\ \boldsymbol{\eta}_S = \eta_S\boldsymbol{I}\,, \tag{2.33}$$

where $\boldsymbol{I}$ is a unit tensor.

While the cantilever dissipation matrix has constant entries, the substrate counterpart should depend on the distance z from the tip to the substrate, and possibly on the lateral coordinates x and y. For the sake of model simplicity, we neglect its x- and y-dependence. We assume the functional form

$$\eta_S(z) = \eta_S^0\left(\frac{\sigma}{z}\right)^{\gamma}, \tag{2.33}$$

where η_S^0 is a constant and the exponent γ is a model parameter. We anticipate that another reasonable choice of this function should not produce any qualitatively different

result, as long as $\eta_S(z)$ decreases with z. We also note that, depending on the normal load, the tip dynamics may be weakly damped or overdamped.

The two main differences between our model and the one from [Wie11] are as follows:

(i) Our model takes into account both dissipation mechanisms, one due to the cantilever and the other due to the substrate, whereas in [Wie11], only the latter dissipation channel is taken into account;

(ii) More importantly, the substrate damping coefficient depends on the distance to the substrate. In contrast, in [Wie11], it is taken to be fixed at the critical damping value $\eta = 2\sqrt{m\kappa}$. It remains unclear why the cantilever elastic response (stiffness κ) should affect the dissipation of energy into the substrate degrees of freedom, as the two processes are unrelated. Even worse, this choice is unphysical, as it predicts dissipation of cantilever energy into the substrate even when the cantilever is far away from the substrate. In our model, on the other hand, the tip damping coefficient assumes the value $\eta_S(z)$ close to the substrate (small z) and η_C far away from it (large z).

Chapter III

Numerical integration of the Langevin equation with a position-dependent damping coefficient

3.1 Formulation of the problem

3.1.1 Langevin equation

We need to numerically simulate the stochastic equations of motion for a particle of mass tensor $\boldsymbol{m}$ under the action of a position- and time-dependent force $\vec{f}(\vec{r},t)$, subject to position-dependent viscous damping with the damping coefficient $\boldsymbol{\eta}(\vec{r})$ and thermal noise $\vec{\xi}(\vec{r},t)$:

$$\boldsymbol{m}\dot{\vec{v}} = \vec{f}(\vec{r},t) - \boldsymbol{\eta}(\vec{r})\vec{v} + \vec{\xi}(\vec{r},t)\ , \qquad \dot{\vec{r}} = \vec{v}\ . \tag{3.1}$$

The second fluctuation-dissipation theorem [Kub66] dictates that the dissipation tensor should be related to the noise autocorrelation as

$$\langle \vec{\xi}(\vec{r}(t),t)\vec{\xi}^{T}(\vec{r}(t'),t')\rangle = 2T\,\boldsymbol{\eta}(\vec{r}(t))\,\delta(t-t')\,, \tag{3.2}$$

where the superscript "*T*" indicates vector transpose.

In numerical integration of Eq. (3.1), the time is discretized into small steps,

$$t \to t_n = n\Delta t, \tag{3.3}$$

and the time derivatives are approximated by the finite-difference expressions like

$$\dot{\vec{v}} \to \frac{\vec{v}_{n+1}-\vec{v}_n}{\Delta t}\,,\ \dot{\vec{r}} \to \frac{\vec{r}_{n+1}-\vec{r}_n}{\Delta t}. \tag{3.4}$$

Such approximations involve the values of the variables on the next time step, which can be found from the values on the previous step using the finite-difference version of the equations of motion (3.1). In this way, the solution of the equations of motion is propagated numerically by any desired time interval in small steps.

Perhaps, the most popular algorithms to integrate Eq. (3.1) numerically in the nanofriction simulations [San01, Nak05, Rot10] are Ermak algorithm [Erm80, All91], and its descendants, such as the Ricci-Ciccotti algorithm [Ric03]. The approach that we are trying to develop in order to numerically integrate Eq. (3.1) should meet certain requirements that are specific to the problem that we are dealing with; both the Ermak and Ricci-Ciccotti approaches do not meet those specifications, as will be explained in the next section.

3.1.2 Applicability in the overdamped limit

The challenging part of our task is that the components of the position-dependent damping tensor $\boldsymbol{\eta}(\vec{r})$ change in a broad range, from almost zero to arbitrarily large values, depending on the distance between the tip and the surface. Hence, our numerical procedure should be applicable both for the weakly damped dynamics and to the overdamped limit of (3.1), formally obtained by setting the mass of the particle to zero, i.e.

$$\boldsymbol{\eta}(\vec{r})\dot{\vec{r}} = \vec{f}(\vec{r},t) + \vec{\xi}(\vec{r},t)\,. \tag{3.5}$$

Physically, the overdamped limit does not mean that our particle is massless (a massless particle should move with the speed of light). Rather, it simply means that the damping term in Eq. (3.1) dominates over the inertia term in the particle's dynamics.

Both Ermak [Erm80] and Ricci-Ciccotti [Ric03] algorithms have been derived for the special case of position-independent damping coefficient, $\eta(x) = \eta$. They differ in how the velocity gets updated on each time step, and how noise is included. In the noise-free case ($T = 0$), both algorithm update the position according to the same second-order expression familiar from kinematics:

$$\vec{r}_{n+1} = \vec{r}_n + \vec{v}_n \Delta t + \frac{\vec{f}_n}{2m} \Delta t^2 \,, \tag{3.8}$$

where $\vec{f}_n = \vec{f}(\vec{r}_n)$. Because the last term diverges in the overdamped limit $m \to 0$, we cannot apply these standard algorithms and must work out a different numerical method.

The second difficulty with the algorithms [Erm80, Ric03] is that they were derived for one-dimensional motion, in which case the dissipation and mass tensors $\boldsymbol{\eta}$ and $\boldsymbol{m}$ are scalars. Updating the velocities according to [Erm80, Ric03] involves multiplication of the previous velocity values with a complicated exponential factor: $v_{n+1} = e^{-\eta \Delta t/m} v_n$ plus force-dependent terms, which also involve $e^{-\eta \Delta t/m}$. It is clear that calculation of the exponential factor may be computationally challenging if both $\boldsymbol{m}$ and $\boldsymbol{\eta}$ are tensors.

3.1.3 Second-order accuracy

The time-step size Δt should be sufficiently small in order to minimize the truncation error associated with the replacement (3.4) of the time derivatives with the finite-difference expressions. On the other hand, the time step cannot be made arbitrarily small. The small time step Δt means that more steps are needed to propagate the solution by a finite time, implying two disadvantages. First, it is the longer overall computational time. Second, it also means accumulation of the numerical round-off error, which is an inevitable side effect of using the finite-precision arithmetic to represent real numbers in computer simulations.

Hence, we require that the truncation error of our numerical procedure should scale with the time-step size as $\mathcal{O}(\Delta t^2)$, i.e. the algorithm should be second-order accurate. This

would allow using a longer time step Δt, implying shorter computational time and better round-off accuracy.

As an illustration, a second-order accurate finite-difference approximation for the value of some function $f(x)$ at a point $x + \Delta x$ is given by the Taylor series truncated after the second term, $f(x + \Delta x) = f(x) + f'(x)\Delta x + \frac{1}{2}f''(x)\Delta x^2$. The finite-difference approximation for the derivative at a point x, $f'(x) = \frac{f(x+\Delta x)-f(x)}{\Delta x}$ [cf. Eq. (3.4)] is only first-order accurate, because the truncation error of this expression is $\frac{1}{2}f''(x)\Delta x$. The conclusion is that the approximations (3.4) are not good approximations for the time derivatives $\dot{\vec{v}}_n$ and $\dot{\vec{r}}_n$ on the time step n.

3.1.4 Stability and numerical test

3.1.4.1 The test system

Before applying our numerical procedure to nanofriction simulation, we need to test it on a simpler system whose dynamics is well understood. Such a system is a one-dimensional noise-free damped harmonic oscillator,

$$m\dot{v} = -\kappa x - \eta v\ , \qquad \dot{x} = v\ . \tag{3.9}$$

The solution of these equations depends on the relation between the natural frequency ω_0 in the absence of damping and the decay constant γ,

$$\omega_0 = \sqrt{\frac{\kappa}{m}}, \gamma = \frac{\eta}{2m}\ . \tag{3.10}$$

In the weakly damped case, $\gamma < \omega_0$, the particle performs damped oscillations with the frequency

$$\omega = \sqrt{\omega_0^2 - \gamma^2}. \tag{3.11}$$

Denoting the initial position and velocity at $t = 0$ as x_i, v_i, the oscillator's position at $t > 0$ is given by

$$x_{exact}(t) = \left(x_i \cos(\omega t) + \frac{v_i+\gamma x_i}{\omega}\sin(\omega t)\right) e^{-\gamma t}\ ,$$

$$v_{exact}(t) = \left(v_i \cos(\omega t) - \frac{\gamma v_i + \omega_0^2 x_i}{\omega} \sin(\omega t)\right) e^{-\gamma t} \tag{3.12}$$

In the opposite strongly damped regime,$\gamma \geq \omega_0$, the particle's coordinate decays to zero according to the two-exponential law

$$x_{exact}(t) = A_+ e^{-\lambda_+ t} + A_- e^{-\lambda_- t} \tag{3.13}$$

with the decay constants and the exponential prefactors given by

$$\lambda_\pm = \gamma \pm \sqrt{\gamma^2 - \omega_0^2}\ ,\ A_\pm = \frac{\lambda_\pm x_i + v_i}{\lambda_\mp - \lambda_\pm}\ . \tag{3.14}$$

3.1.4.2 Numerical stability

Because the test system is linear, the numerical procedure used to simulate it is linear as well. Combining the particle's velocity and position on the n^{th} time step into a single state vector

$$\underline{y}_n = (v_n, x_n)\ , \tag{3.15}$$

the next value of the state vector is obtained as

$$\underline{y}_{n+1} = \boldsymbol{J}\, \underline{y}_n\ , \tag{3.16}$$

where the 2×2 matrix $\boldsymbol{J}$ depends on the numerical procedure employed to simulate (3.9) Let $\underline{e}_n$ be the round-off error vector, i.e. the difference between the approximate solution obtained by propagating this numerical equation by n steps and the result that would have been obtained if the computer arithmetic had been infinitely precise, i.e. if the numbers had been represented by infinitely many significant figures. In view of the linearity of (3.16), the error propagates according to the same law,

$$\underline{e}_{n+1} = \boldsymbol{J}\, \underline{e}_n\ . \tag{3.17}$$

Now, the 2×2 matrix $\boldsymbol{J}$ has two eigenvalues, which we denote as μ_1 and μ_2, and two mutually orthogonal eigenvectors, denoted as $\underline{u}_1$ and $\underline{u}_2$, such that

$$\boldsymbol{J}\, \underline{u}_i = \mu_i \underline{u}_i \ \text{ and } \underline{u}_i \cdot \underline{u}_j = \delta_{ij}. \tag{3.18}$$

Hence, the error vector on the *nth* step is related to the initial error $\underline{e}_0$ by $\underline{e}_n = \sum_{i=1}^{2} \mu_i^n\, (\underline{u}_i^T\, \underline{e}_0)\, \underline{u}_i$, as can be verified by direct substitution. The conclusion is that the error will grow exponentially with each time step if the matrix $\boldsymbol{J}$ has at least one

eigenvalue whose real part exceeds unity in magnitude. Hence, the stability condition of a numerical procedure is:

$$|Re(\mu_i)| < 1 \text{ for all } i \, . \tag{3.19}$$

For notational simplicity, in this chapter we will discuss the one-dimensional version of the equations of motion (3.1), namely,

$$m\dot{v} = f(x,t) - \eta(x)v + \sqrt{2\eta(x)T}\xi(t) \, , \qquad \dot{x} = v \, , \tag{3.20}$$

where the white-noise Gaussian process $\xi(t)$ has the properties $\langle \xi(t) \rangle = 0$ and $\langle \xi(t)\xi(t') \rangle = \delta(t-t')$. The algorithm obtained for the one-dimensional dynamics (3.20) will then be generalized to higher dimensions in the end.

3.2 Leapfrog algorithm

3.2.1 Undamped noise-free particle

Consider the one-dimensional motion of a particle of mass m under the action of a position- and time-dependent force $f(x,t)$ in the absence of noise and dissipation:

$$m\dot{v} = f(x,t) \, , \qquad \dot{x} = v \, . \tag{3.21}$$

A standard method to simulate these equations numerically is to use the leap-frog algorithm, see chap. 4.3.1 of [Fre96]. We first observe that the second ratio (3.1.4) is a second-order approximation for the velocity $v_{n+1/2}$ at the moment of time $t_{n+1/2} = (n + 1/2)\Delta t$. Indeed, considering the Taylor expansion of the coordinate, around the time $t_{n+1/2}$, we have:

$$x_{n+1} = x_{n+1/2} + v_{n+1/2}\frac{\Delta t}{2} + \frac{1}{2}\dot{v}_{n+1/2}\frac{\Delta t^2}{4} + \frac{1}{6}\ddot{v}_{n+1/2}\frac{\Delta t^3}{8} + \cdots \, , \tag{3.22}$$

$$x_n = x_{n+1/2} - v_{n+1/2}\frac{\Delta t}{2} + \frac{1}{2}\dot{v}_{n+1/2}\frac{\Delta t^2}{4} - \frac{1}{6}\ddot{v}_{n+1/2}\frac{\Delta t^3}{8} + \cdots \, . \tag{3.23}$$

Subtracting the two equations from each other and dividing by Δt, we find:

$$v_{n+1/2} = \frac{x_{n+1}-x_n}{\Delta t} - \ddot{v}_{n+\frac{1}{2}}\frac{\Delta t^2}{24} + \cdots = \frac{x_{n+1}-x_n}{\Delta t} + \mathcal{O}(\Delta t^2). \tag{3.24}$$

The leading-order term neglected in the truncated expression (3.24) is of the second order.

A similar reasoning applies to the acceleration $a = \dot{v}$, giving for $a_n = \frac{1}{m} f_n$ the expression

$$a_n = \frac{v_{n+1/2} - v_{n-1/2}}{\Delta t} - \ddot{a}_n \frac{\Delta t^2}{24} + \cdots . \tag{3.25}$$

We thus arrive at the second-order accurate discretized version of (3.21)

$$\frac{v_{n+1/2} - v_{n-1/2}}{\Delta t} = \frac{f_n}{m} + \mathcal{O}(\Delta t^2) , \ \frac{x_{n+1} - x_n}{\Delta t} = v_{n+1/2} + \mathcal{O}(\Delta t^2) . \tag{3.26}$$

In the leap-frog algorithm, the velocity and coordinate are updated sequentially. That is, the new velocity value is found first according to

$$v_{n+1/2} = v_{n-1/2} + f_n \frac{\Delta t}{m} + \mathcal{O}(\Delta t^3) , \tag{3.27}$$

and then the coordinate gets updated based on this new velocity value:

$$x_{n+1} = x_n + v_{n+1/2} \Delta t + \mathcal{O}(\Delta t^3) . \tag{3.28}$$

Leapfrog is second-order accurate because, propagation of these discretized equations by a finite time t consists of $t/\Delta t$ time steps; hence, the truncation error scales as $\mathcal{O}(\Delta t^3) t/\Delta t \sim O(\Delta t^2)$.

3.2.2 Leapfrog algorithm for a damped particle

Now, we attempt to generalize the leapfrog approach by including the damping effect into the equations of motion (3.21):

$$m\dot{v} = f(x,t) - \eta(x) v, \ \dot{x} = v . \tag{3.29}$$

To preserve the second-order accuracy of the leapfrog algorithm (3.27), (3.28), the force in the right-hand side of the first equation (3.29) must be taken on the n^{th} time step, whereas the acceleration should be approximated as $(v_{n+1/2} - v_{n-1/2})/\Delta t$. The problem is that the force depends on the velocity via the dissipation term, $-\eta(x)v$, which should change to $-\eta_n v_n$ in a finite-difference scheme, where $\eta_n = \eta(x_n)$. But in the leapfrog algorithm, the velocity is evaluated on the half-integer time steps.

The obvious way around this difficulty is to take an average between $v_{n+1/2}$ and $v_{n-1/2}$ in the dissipation term $-\eta_n v_n$. Indeed, let us express the velocities $v_{n+1/2}$ and $v_{n-1/2}$ as the Taylor series:

$$v_{n\pm1/2} = v_n \pm \dot{v}_n \frac{\Delta t}{2} + \frac{1}{2}\ddot{v}_n \frac{\Delta t^2}{4} + \cdots . \tag{3.30}$$

Taking the arithmetic average between $v_{n+1/2}$ and $v_{n-1/2}$ we obtain a second-order accurate approximation:

$$v_n = \frac{v_{n-1/2}+v_{n+1/2}}{2} + \cdots . \tag{3.31}$$

The error of this approximation is $-\ddot{v}_n \Delta t^2/8$ in the leading order. Using this expression in the finite-difference representation of (3.29), we obtain:

$$\begin{aligned} &\frac{v_{n+1/2}-v_{n-1/2}}{\Delta t} = \frac{f_n}{m} - \eta_n \frac{v_{n-1/2}+v_{n+1/2}}{2} + \mathcal{O}(\Delta t^2) , \\ &\frac{x_{n+1}-x_n}{\Delta t} = v_{n+1/2} + \mathcal{O}(\Delta t^2) . \end{aligned} \tag{3.32}$$

Solving the first equation for $v_{n+1/2}$, we derive the leapfrog algorithm for a damped particle in the absence of noise:

$$\begin{aligned} &v_{n+1/2} = \frac{2m-\eta_n \Delta t}{2m+\eta_n \Delta t} v_{n-1/2} + \frac{2\Delta t}{2m+\eta_n \Delta t} f_n + \mathcal{O}(\Delta t^3) , \\ &x_{n+1} = x_n + v_{n+1/2}\Delta t + \mathcal{O}(\Delta t^3) . \end{aligned} \tag{3.33}$$

The pleasant feature of the algorithm (3.33) is that it remains second-order accurate in the overdamped limit. Indeed, setting $m = 0$, we have:

$$\begin{aligned} &v_{n+1/2} = -v_{n-1/2} + \frac{2}{\eta_n} f_n + \mathcal{O}(\Delta t^3) , \\ &x_{n+1} = x_n + v_{n+1/2}\Delta t + \mathcal{O}(\Delta t^3) . \end{aligned} \tag{3.34}$$

Combining both expressions and using the fact that $v_{n-1/2} = \frac{x_n - x_{n-1}}{\Delta t}$, we have

$$x_{n+1} = x_{n-1} + \frac{2\Delta t}{\eta_n} f_n + \mathcal{O}(\Delta t^3) . \tag{3.35}$$

This is a second-order accurate finite-difference representation of an overdamped equation of motion $\eta(x)\dot{x} = f(x,t)$, obtained by approximating the time derivative at the n^{th} step by $\dot{x}_n = \frac{x_{n+1}-x_{n-1}}{2\Delta t}$.

3.2.3 Stability test

Let us now apply our generalized leapfrog formulas (3.33) to the test system (3.9) from Section 3.1.4. In the zero-damping limit, it becomes the standard leapfrog scheme

$$v_{n+1/2} = v_{n-1/2} - \frac{\kappa \Delta t}{m} x_n \,,$$

$$x_{n+1} = x_n + v_{n+1/2}\Delta t = x_n + \left(v_{n-1/2} - \frac{\kappa \Delta t}{m} x_n\right)\Delta t \,, \tag{3.36}$$

which can be written in the matrix form

$$\begin{pmatrix} v_{n+1/2} \\ x_{n+1} \end{pmatrix} = \boldsymbol{J} \begin{pmatrix} v_{n-1/2} \\ x_{n-1} \end{pmatrix} = \begin{pmatrix} 1 & -\kappa \Delta t/m \\ \Delta t & 1 - \kappa \Delta t^2/m \end{pmatrix} \begin{pmatrix} v_{n-1/2} \\ x_n \end{pmatrix}. \tag{3.37}$$

The eigenvalues of the matrix $\boldsymbol{J}$ are found from the secular equation $\det(\boldsymbol{J} - \mu \boldsymbol{I}) = 0$, where $\boldsymbol{I}$ is a unit matrix. They are:

$$\mu_{1,2} = 1 - \frac{\omega_0^2 \Delta t^2}{2} \pm \frac{\omega_0^2 \Delta t^2}{2} \sqrt{1 - \frac{4}{\omega_0^2 \Delta t^2}} \,, \tag{3.38}$$

where $\omega_0 = \sqrt{\kappa/m}$ is the natural angular frequency of oscillations (3.10). If the time step is small enough, namely,

$$\Delta t < 2/\omega_0 = T_{osc}/\pi \,, \tag{3.39}$$

$T_{osc} = 2\pi/\omega_0$ being the oscillation period, the square root becomes an imaginary number and both eigenvalues have the real part satisfying the inequality

$0 < Re(\mu_{1,2}) < 1$.

The leapfrog scheme is thus stable in the undamped limit.

Surprisingly, in spite of its second-order accuracy, this algorithm is numerically unstable in the overdamped limit. Indeed, with $f_n = -\kappa x_n$, equations (3.34) can be written as

$$v_{n+1/2} = -v_{n-1/2} - \frac{2\kappa}{\eta_n} x_n \,,$$

$$x_{n+1} = x_n + v_{n+1/2}\Delta t = x_n - \left(v_{n-1/2} + \frac{2\kappa}{\eta_n} x_n\right)\Delta t \,. \tag{3.40}$$

In the matrix form (3.36), this is formulated as

$$\begin{pmatrix} v_{n+1/2} \\ x_{n+1} \end{pmatrix} = \boldsymbol{J} \begin{pmatrix} v_{n-1/2} \\ x_{n-1} \end{pmatrix} = \begin{pmatrix} -1 & -2\kappa/\eta \\ -\Delta t & 1 - 2\kappa \Delta t/\eta \end{pmatrix} \begin{pmatrix} v_{n-1/2} \\ x_n \end{pmatrix}, \tag{3.41}$$

and the eigenvalues of $\boldsymbol{J}$ are:

$$\mu_{1,2} = -\frac{\kappa\Delta t}{\eta} \pm \sqrt{\left(\frac{\kappa\Delta t}{\eta}\right)^2 + 1}\,. \tag{3.42}$$

The eigenvalue with the minus sign in front of the square root is $\mu_2 < -1$, i.e. $|\mu_2| > 1$. The approximation (3.32) will therefore break down if damping is high.

3.3 The combined algorithms

3.3.1 LE algorithm: Combining the Leapfrog and Ermak schemes

The root of the failure of the algorithm (3.30) considered above is in the approximation (3.31) for the damping force $-\eta_n v_n$. But the main *idea* of the leap-frog algorithm from section 3.2.1 is still valid. This idea is:

treat the coordinate x_n as constant when updating the velocity;

treat the velocity $v_{n+1/2}$ as constant when updating the coordinate.

This idea was first explicitly formulated in Ermak and Buckholtz numerical treatment of the Langevin equation with damping [Erm80].

Armed with this observation, we consider the equation for velocity (3.29) on the time interval $(t_{n-1/2}, t_{n+1/2})$ with a constant coordinate $x = x_n$:

$$m\dot{v}(t) = f_n - \eta_n v(t) \tag{3.43}$$

with the initial condition $v(t_{n-1/2}) = v_{n-1/2}$. The solution reads:

$$v(t) = e^{-\eta_n (t - t_{n-1/2})/m} v_{n-1/2} + \frac{f_n}{\eta_n}\left(1 - e^{-\eta_n (t - t_{n-1/2})/m}\right). \tag{3.44}$$

Setting t to $t_{n+1/2}$, we obtain the updated velocity, whereas the coordinate gets updated according to the same formula (3.34):

$$v_{n+1/2} = e^{-\eta_n \Delta t/m} v_{n-1/2} + \frac{f_n}{\eta_n}\left(1 - e^{-\eta_n \Delta t/m}\right),$$

$$x_{n+1} = x_n + v_{n+1/2}\Delta t. \tag{3.45}$$

The Ermak-Buckholtz scheme [Erm80] is similar to (3.45) in that it also involves the factors like $e^{-\eta_n \Delta t/m}$. The important difference between [Erm80] and the present treatment is that, in Ermak's scheme, coordinates and velocities are evaluated on the same

time step. Therefore, Ermak's scheme is formally quite different from (3.45). Nonetheless, because the idea first proposed in [Erm80] was used to derive (3.45), the scheme (3.45) will be referred to as Leapfrog- Ermak (LE) scheme hereafter.

In the limit of zero damping $\eta \to 0$, this scheme reduces to the second-order accurate leapfrog scheme (3.27), (3.28). In the opposite limit of overdamped motion $m \to 0$, this scheme turns into the Euler scheme:

$$v_{n+1/2} = \frac{f_n}{\eta_n}\,,\ x_{n+1} = x_n + v_{n+1/2}\Delta t = x_n + \frac{f_n}{\eta_n}\Delta t\,, \tag{3.46}$$

which is only a first-order accurate finite-difference representation of the dynamics $\eta(x)\dot{x} = f(x)$.

It comes as a slight surprise that the accuracy of the LE scheme (3.45) in the overdamped limit is worse than the second-order accuracy of the algorithm (3.35). After all, to obtain the second-order expression (3.15), an *approximation* (3.31) was made for the viscous force. On the other hand, this force was treated *rigorously* to derive the LE scheme (3.45).

This loss of accuracy can be considered as the price paid for the stability of the algorithm at high damping. Focusing on the model (3.29) in the overdamped limit $m \to 0$, our LE scheme reduces to the simple Euler algorithm (3.46), that is, $x_{n+1} = x_n\left(1 - \frac{\kappa}{\eta}\Delta t\right)$. It is stable provided that

$$\Delta t < \eta/\kappa. \tag{3.47}$$

In the undamped limit $\eta \to 0$, the LE algorithm (3.45) turns into the standard leapfrog scheme, which is both stable (see Section 3.2.3) and second-order accurate (see Section 3.2.1).

Stability analysis in the general case when both dissipation and inertia are present is tedious and is not performed here. But it is intuitively clear that the algorithm should be stable in this case provided that the time step is reasonably small.

3.3.2 Leapfrog (semi-)implicit (LI) algorithm

The numerical procedure (3.45) presented above is not the only possible one which turns into the standard leapfrog method at zero damping and to Euler method in the overdamped limit. A simpler alternative can be found by following the same steps that have led us to the leapfrog scheme from Section 3.2.2, which turned out to be unstable in the overdamped limit. A simple "trick" to turn it into a stable numerical procedure is to use, instead of the second-order accurate approximation (3.31) for the damping term $-\eta v$, a first-order accurate combination $-\eta_n v_{n+1/2}$. This leads to the finite-difference version of Eq. (3.29):

$$\begin{aligned} m\frac{v_{n+1/2}-v_{n-1/2}}{\Delta t} &= f_n - \eta_n v_{n+1/2}\ , \\ \frac{x_{n+1}-x_n}{\Delta t} &= v_{n+1/2}\ . \end{aligned} \tag{3.48}$$

which is first-order accurate, unless the damping term is zero. The right-hand side of the first equation depends on the "new" velocity value. A numerical procedure in which the new values of the system's variables are used to update those variables is called implicit (see Chapter 16.6 of [Pre99]). Hence, this procedure can be termed leapfrog implicit (more precisely, semi-implicit) method. The algorithm is:

$$\begin{aligned} v_{n+1/2} &= \frac{m}{m+\eta_n \Delta t} v_{n-1/2} + \frac{\Delta t}{m+\eta_n \Delta t} f_n\ , \\ x_{n+1} &= x_n + v_{n+1/2}\Delta t. \end{aligned} \tag{3.49}$$

3.3.3 Comparison between the LE and LI procedures

At a first glance, the LE scheme (3.45), in which the damping term has been treated rigorously, should outperform the LI procedure (3.49), in which the damping term was approximated as $-\eta_n v_{n+1/2}$. To see if this is the case, we simulate the dynamics of a simple harmonic oscillator (3.9). Because both algorithms agree with each other in the overdamped limit, it makes sense to focus on the case of weak damping (3.12). Consequently, we take $m = 1$, $\kappa = 1$, and $\eta = 0.1$.

In the simulations presented below, the initial coordinate value was set to $x_i = 0$ and the initial velocity $v_i = 1$. The time step was set to $\Delta t = 0.01$. Correspondingly, the starting position was $x_0 = x_i$ at the moment $t_0 = 0$. Since in both LI and LE methods the velocity

is evaluated at half-integer time steps, the initial velocity was set to $v_{1/2} = v_{exact}(\Delta t/2)$, where the exact velocity expression is provided by the second equation (3.12).

To compare between the LI and LE methods, we look at the behavior of the energy,

$$E(t) = \frac{\kappa x^2(t)}{2} + \frac{mv^2(t)}{2} \tag{3.50}$$

The exact energy is obtained with the help of Eq. (3.12). The numerical counterpart on the time step t_n was determined as

$$E_n = \frac{\kappa x_n^2}{2} + \frac{m}{2}\left(\frac{v_{n-1/2}+v_{n+1/2}}{2}\right)^2 . \tag{3.51}$$

Presented in Figure 3.1 is the error in the energy determination according to the LE and LI schemes, defined as $|E_n - E_{exact}(t_n)|$. It is obvious from Figure 3.1 that both methods result in very similar energy values, deviating from the exact energy by about 1%. Taking smaller time step improves the accuracy of such calculations.

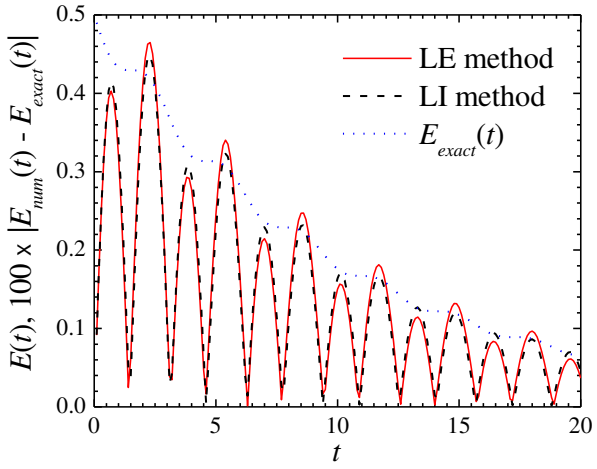

Figure 3.1: Numerical error in the energy determined using the LE (red solid line) and LI (black dashed line) algorithms for the system described in Section 3.3.3 The blue dotted line shows the temporal evolution of the oscillator's energy. For the ease of comparison, the energy error is magnified by a factor of 100.

We have performed extensive simulations for other parameter values and initial conditions, with the conclusion that the leapfrog-Ermak algorithm does not offer any accuracy improvement as compared to the leapfrog-implicit algorithm.

At the same time, the LI procedure (3.49) is simpler than the LE procedure (3.45). This is not an important factor when the two algorithms are applied to a simple one-dimensional damped oscillator (3.9). However, for higher-dimensional systems, the damping coefficient η becomes a tensor $\boldsymbol{\eta}$. Hence, evaluation of the matrices like $e^{-\boldsymbol{m}^{-1}\boldsymbol{\eta}_n\Delta t}$ in Eq. (2.23) on each time step will become a non-trivial problem, unless the tensor $\boldsymbol{\eta}$ is diagonal. Finding the inverse matrix $(\boldsymbol{m}I + \boldsymbol{\eta_n}\Delta t)^{-1}$, as required by Eq. (3.49) of the LI algorithm, is in fact even not necessary in numerical simulations, see Section 3.5 below. Therefore, in the simulations of the Langevin equation, the leapfrog implicit method (3.49) is the method of choice.

3.4 Including the noise

3.4.1. Noise correlation

Our final task is to incorporate Gaussian white noise into our numerical scheme (3.49). Because the noise term in (3.1) is Gaussian, white, and unbiased, we include it as a Gaussian random variable in (3.49):

$$v_{n+1/2} = \frac{m}{m+\eta_n\Delta t}\, v_{n-1/2} + \frac{\Delta t}{m+\eta_n\Delta t}\,(f_n + \xi_n)\,, \quad x_{n+1} = x_n + v_{n+1/2}\Delta t. \tag{3.52}$$

This variable enjoys the properties

$$\langle \xi_n \rangle = 0\,,\ \langle \xi_n \xi_{n'} \rangle = \langle \xi_n^2 \rangle \delta_{nn'}\,. \tag{3.53}$$

Numerical generation of a Gaussian random variable ξ_n can be accomplished, e.g., using the C function gasdev from Chapter 7.2 of the Numerical Recipes [Pre99]. It remains to determine its variance $\langle \xi_n^2 \rangle$.

Noise properties should not depend on the mass of the particle and on the external potential in which the particle finds itself. Therefore, to establish $\langle \xi_n^2 \rangle$, we may focus on the overdamped limit of (3.52) with $f_n = 0$. Within the time interval (t_n, t_{n+1}), we first replace in the overdamped Langevin equation $\eta(x) \to \eta(x_n) = \eta_n$ and $\xi(x,t) \to \xi(t)$:

$$\eta_n \dot{x}(t) = \xi(t) \tag{3.54}$$

with

$$\langle \xi(t) \rangle = 0 \text{ and } \langle \xi(t)\xi(t') \rangle = 2T\eta_n \delta(t'-t), \text{ where both } t, t' \in (t_n, t_{n+1}) \, . \tag{3.55}$$

Time-integration of (3.54) from t_n to t_{n+1} gives $\Delta x_{n+1} = x_{n+1} - x_n = \frac{1}{\eta_n} \int_{t_n}^{t_{n+1}} dt \, \xi(t)$. Squaring both sides and averaging over all possible noise realizations according to (3.55), we recover the diffusion law

$$\langle \Delta x_{n+1}^2 \rangle = \frac{1}{\eta_n^2} \iint_{t_n}^{t_{n+1}} dt \, dt' \, \langle \xi(t)\xi(t') \rangle = \frac{2T}{\eta_n} \iint_{t_n}^{t_{n+1}} dt \, dt' \, \delta(t'-t) = 2\frac{T}{\eta_n} \Delta t \tag{3.56}$$

which gives the Einstein's relation for the diffusion coefficient $D_n = T/\eta_n$.

Turning to the finite-difference version of Eq. (3.54), we have

$$\eta_n \frac{\Delta x_{n+1}}{\Delta t} = \xi_n \, , \langle \Delta x_{n+1}^2 \rangle = \frac{\Delta t}{\eta_n} \langle \xi_n^2 \rangle \, . \tag{3.57}$$

Comparison of the last two expression yields:

$$\langle \xi_n^2 \rangle = \frac{\langle \Delta x_{n+1}^2 \rangle}{\Delta t} = \frac{2\eta_n T}{\Delta t} \, . \tag{3.58}$$

The expression (3.58) was derived by considering the overdamped regime of motion. Hence, it may become erroneous if we go beyond the overdamped limit. To see if this is the case, consider the mean-squared velocity of the particle in thermal equilibrium, $\langle v_{n-1/2}^2 \rangle = \langle v_{n+1/2}^2 \rangle = \langle v_{eq}^2 \rangle$. Assuming for simplicity zero force, $f_n = 0$, we obtain from (3.52):

$$\langle v_{eq}^2 \rangle = \frac{m^2}{(m+\eta_n \Delta t)^2} \langle v_{eq}^2 \rangle + \frac{\Delta t^2}{(m+\eta_n \Delta t)^2} \langle \xi_n^2 \rangle \, . \tag{3.59}$$

Combining this with (3.58) and performing simple algebraic manipulations, we obtain:

$$\langle v_{eq}^2 \rangle = \frac{T}{m+\eta_n \Delta t/2} \, . \tag{3.60}$$

This result underestimates the exact value $\langle v_{eq}^2 \rangle = \frac{T}{m}$ expected from the equipartition theorem by a factor $1 + \eta_n \Delta t/(2m)$. In order for the associated error in the mean kinetic energy to be small, the time step must be much smaller than the value

$$\Delta t \ll \frac{2m}{\eta_n} . \tag{3.61}$$

3.5. Generalization to higher dimensions

We now generalize the LI algorithm (3.49) to the multidimensional Langevin equation (3.1), which is written in the finite-difference form as

$$\boldsymbol{m}\frac{\vec{v}_{n+1/2}-\vec{v}_{n+1/2}}{\Delta t} = \vec{f}_n - \boldsymbol{\eta}_n \vec{v}_{n+1/2} + \vec{\xi}_n , \qquad \frac{\vec{r}_{n+1}-\vec{r}_n}{\Delta t} = \vec{v}_{n+1/2} . \tag{3.62}$$

The generalization of Eq. (3.58) to higher dimensions reads

$$\langle \vec{\xi}_n \vec{\xi}_n^T \rangle = \frac{2T}{\Delta t}\boldsymbol{\eta}_n , \tag{3.63}$$

where $\vec{\xi}_n^T$ is the transpose of a random vector $\vec{\xi}_n$.

Rearranging the terms in the first equation (3.62), we obtain:

$$(\boldsymbol{m} + \boldsymbol{\eta}_n \Delta t)\vec{v}_{n+1/2} = \boldsymbol{m}\vec{v}_{n+1/2} + \Delta t(\vec{f}_n + \vec{\xi}_n) . \tag{3.64}$$

Hence, the new velocity vector $\vec{v}_{n+1/2}$ is found by solving a system of linear equations of the form $\boldsymbol{A}\vec{v}_{n+1/2} = \vec{b}$, where the matrix $\boldsymbol{A} = \boldsymbol{m} + \boldsymbol{\eta}_n \Delta t$ that multiplies the unknown vector is positive definite and symmetric.

The most efficient way to solve this system is to perform a Cholesky decomposition of this matrix, in which the matrix is represented by a product of a lower triangular matrix and its transpose:

$$\boldsymbol{A} = \boldsymbol{L}\boldsymbol{L}^T . \tag{3.65}$$

The new velocity is found by first solving the system $\boldsymbol{L}\vec{c} = \vec{b}$ for an auxiliary vector $\vec{c} = \boldsymbol{L}^T \vec{v}_{n+1/2}$, and then solving the last relation for $\vec{v}_{n+1/2}$. In view of the fact that $\boldsymbol{L}$ and $\boldsymbol{L}^T$ are triangular matrices, these two steps are computationally simple.

To generate the entries of a Gaussian random vector $\vec{\xi}_n$ with zero mean and the covariance (3.63), we employ a procedure first suggested by Ermak and McCammon [Erm78]. Namely, we first present them as a linear combination

$$\vec{\xi}_n = \boldsymbol{C}_n \vec{\zeta}, \tag{3.66}$$

where the entries of a random vector $\vec{\zeta}$ are independent Gaussian random numbers with zero mean and unit variance:

$$\langle \vec{\zeta} \rangle = 0, \langle \vec{\zeta} \vec{\zeta}^T \rangle = \boldsymbol{I}. \tag{3.67}$$

Substitution of (3.66) into (3.63) using the property (3.67) gives:

$$\boldsymbol{C}_n \boldsymbol{C}_n^T = \frac{2T}{\Delta t} \boldsymbol{\eta}_n \,, \tag{3.68}$$

i.e. the matrix $\boldsymbol{C}_n$ is directly related to the Cholesky decomposition of the positive-definite symmetric matrix $\boldsymbol{\eta}_n$.

A standard algorithm for Cholesky decomposition (3.65), (3.68) can be found in the literature, see e.g. Chapter 2.9 of [Pre99].

Chapter IV

Results and Discussion

4.1 Parameter values

4.1.1 Units

To describe a physical system, it is desirable to use those units in which the numerical values of all the relevant parameters are not too big and not too small. In the context of nanofriction, the following basic units of length, force, and mass are experimentally convenient:

$[L]$ = nm, $[f]$ = nN, $[m]$ = ng .

From these, the units of energy and time are derived as

Table 4.1: Cantilever parameters used in the calculations

Parameter name and symbol	**Literature values**	**Value used**
Normal stiffness, κ_N	0.05 nN/nm [Soc04, Sch06]; 0.12 nN/nm [Sch05]; 0.14 [Jan10], 0.2 nN/nm [Evs06]; 0.35 nN/nm [Rie03]	0.1 nN/nm
Lateral stiffness, κ_L	6 nN/nm [Sch06]; 12.7 [Jan10]; 14 nN/nm [Sch05]; 16.5 nN/nm [Ben99]; 19 nN/nm [Evs06]; 50 nN/nm [Sch06]; 75 nN/nm [Rie03]	10 nN/nm
Normal mass, m_N	5.5 ng [Rie03]; 7.6 ng [Lan10]	6 ng
Lateral mass, m_L	30 ng [Rie03, Mer15], 55 ng [Mai05]	30 ng
Damping coefficient, η_C	Normal: $1.4 \cdot 10^{-4}$ ng/μs [Lan10], $5.7 \cdot 10^{-3}$ [Yuy11] Lateral: $3 \cdot 10^{-6}$ ng/μs [Mai05]	10^{-3} ng/μs

$[E]$ = nN·nm = aJ, $[t]$ = (ng·nm/nN)^{½} = μs .

In particular, the thermal energy at 300 K is k_BT = $4.14 \cdot 10^{-3}$ aJ. The typical pulling velocity in an AFM experiment covers the range between 0.001 and 10 μm/s [Rie03], corresponding to the range between 10^{-6} and 10^{-2} nm/μs in the units adopted.

In this section, we will not attempt to quantitatively reproduce any particular set of experimental results from the literature. Rather, we will focus on those parameter values that are typical for the majority of nanofriction experiments reported. In this way, our simulation results are in reasonably, although not perfect agreement with the published data that we are aware of.

4.1.2 Cantilever properties

The properties of the cantilever adopted in this thesis are summarized in the third column of the Table 1. Cantilever normal and lateral masses were estimated based on the resonance frequency, $\nu_{res} = \frac{1}{2\pi}\sqrt{\frac{\kappa}{m}}$, and the spring constant. The resonance frequency for normal and lateral oscillations of a free cantilever are [Rie03] $\nu_{res,N} = 40$ kHz and $\nu_{res,L} = 250$ kHz. Using the normal and the lateral stiffness from [Rie03], namely, $\kappa_N = 0.35$ nN/nm and $\kappa_L = 75$ nN/nm, we obtain the estimates for the normal and the lateral masses of 5.5 ng and 30 ng, respectively.

Table 4.2: Substrate parameters used in the calculations

Parameter	a	σ	ε	β	h	η_S^0	γ
Value used	0.3 nm	0.3 nm	10 aJ	2	0.02	1 ng/μs	2

The damping coefficient η_C was deduced from the cantilever quality factor, defined as $Q = \frac{2\pi f_{res}}{\eta}$. In principle, we could have used different values for the normal and lateral damping coefficients. However, when the cantilever is in contact with the substrate, its energy dissipation is determined primarily by the substrate degrees of freedom. Hence, the torsional dissipation in the cantilever plays little role as compared to substrate dissipation, allowing us to set the respective damping coefficient to its normal counterpart.

4.1.3 Substrate potential and dissipation parameters

While the cantilever parameters can be established relatively easily from the literature, determination of its interaction properties with the substrate is not as unambiguous. The experimental parameters that are usually reported are the adhesion force, i.e. the maximal force generated by the tip-substrate potential, and the effective spring constant, i.e. the slope of the lateral force vs. cantilever base positon curve in the stick phases. At the same

time, we have 6 parameters in the potential (II.2.14): a, σ, ε, β, h. These values are summarized in Table 4.2.

The values $a = \sigma = 0.3$ nm are typical interatomic distances in a solid. The exponent β is set to 2 somewhat arbitrarily, but we have verified by explicit calculations that the results reported below do not change qualitatively if other values of β are chosen.

The substrate-tip interaction energy is selected so as to correctly reproduce the adhesion force, i.e. the largest tip-substrate interaction force on the tip generated by the substrate. According to Eq. (II.2.12), the force generated by the substrate is

$$-\frac{dU_0(z)}{dz} = \frac{\varepsilon}{\sigma}\frac{\beta}{\beta-1}\left(\frac{\sigma}{z}\right)^2\left[\left(\frac{\sigma}{z}\right)^{\beta-1} - 1\right]. \tag{4.1}$$

By finding the maximum, z_{max}, of this function, we determine the adhesion force as

$$z_{max} = \sigma\left(\frac{\beta+1}{2}\right)^{1/(\beta-1)}, \quad f_{adh} = \left.\frac{dU_0}{dz}\right|_{z=z_{max}} \tag{4.2}$$

The experimental adhesion force values reported in the literature range from 0.7 nN [Soc04], 11 nN [Sch05], 15 nN [Ben99], to ca. 45 nN [Gos11]. The value $\varepsilon = 10$ aJ gives $f_{adh} = 9.88$ nN, which is comparable to the experimental values.

It remains to make a choice for the values of the corrugation parameter h and the parameters η_S^0 and γ of the substrate dissipation coefficient (II.2.19). We assume that the damping exponent has the same value as the corrugation exponent, $\gamma = 2$, because both damping and corrugation are produced by the atoms of the same substrate. To make a reasonable choice of the corrugation parameter h, we note that the typical force against the lateral motion of the tip is of the order of $\varepsilon h/a$. Setting $h = 0.02$ makes it of the order of 0.7 nN, which is typical in an experiment [Sch05, Ben99]. Finally, we employ an experimental observation that the damping coefficient of the cantilever in contact with the substrate is 10^2-10^3 times as high as the free cantilever counterpart [Mai05, Soc06], allowing us to take $\eta_S^0 = 1$ ng/μs.

4.2 Friction without cantilever actuation

4.2.1 Stick-slip motion

Shown in Figure 4.1 is the (a) lateral and (b) normal force developed in the cantilever as it is pulled along the (100) direction of the substrate at velocity $V = 10^{-6}$ nm/μs (black dashed line) and 10^{-3} nm/μs (green solid line) at temperature T=0k. In both cases, the force evolves in a manner typical for the stick-slip motion. At fast pulling velocity, both lateral and normal force exhibit the "ring-down" effect after each slip event. At slower pulling, the ring-down oscillations are also present, but they decay too fast to be seen in the friction vs. cantilever base position plot. It is seen in Figure 4.1 that at $V = 10^{-6}$ nm/μs, about 20 ring-down oscillations occur as the cantilever base travels about $\Delta X = 0.15$ nm. This corresponds to the temporal period of

$$\frac{1}{\nu_{ringdown}} = \frac{\Delta X}{20V} = \frac{0.15\ \text{nm}}{20 \cdot 10^{-6}\text{nm}/\mu\text{s}} = 7.5\ \mu\text{s},$$

or the frequency of $\nu_{ringdown} = 133\ \text{kHz} = 0.133\ \mu\text{s}^{-1}$. This value agrees with the torsional resonance frequency of the cantilever, $\nu_{L,res} = \frac{1}{2\pi}\sqrt{\frac{\kappa_L}{m_L}} = 92\ \text{kHz}$ with the parameter values from Table 1. Such ring-down oscillations have been reported in at least one experimental paper [Fel16], although the ring-down frequency reported in [Fel16] is about 50 to 80 times as small as our value ($\nu_{ringdown} = 1.5 - 3\ \text{kHz}$ according to [Fel16]).

The normal force of the cantilever exhibits very little variation of only about 0.002% as the tip is pulled along the substrate. The normal force can be related to the tip base position Z by an approximate formula

$$\langle f_N \rangle \approx \kappa_N(-Z + \sigma)\ . \tag{4.3}$$

This relation follows with $z \approx \sigma$ from equation (2.23).

The accuracy of this approximation is better than 0.1%.

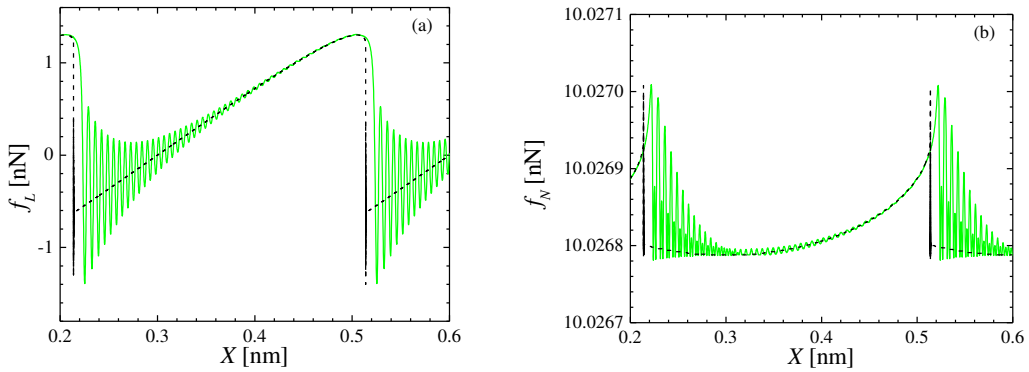

Figure 4.1: (a) Lateral and (b) normal force for pulling in the (100) direction at the pulling velocity $V = 10^{-6}$ nm/μs (black curves) and 10^{-3} nm/μs (green curves) at the cantilever base position $Z = -100$ nm.

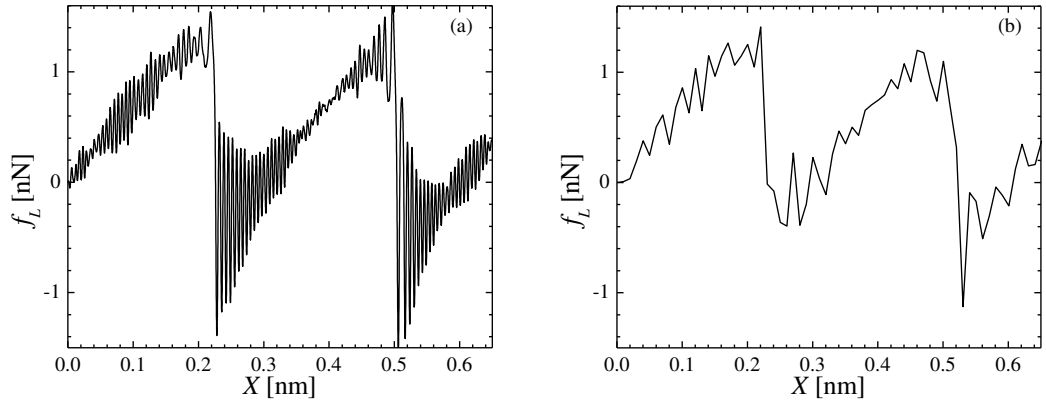

Figure 4.2: Lateral force for pulling in the (100) direction at the pulling velocity $V = 10^{-6}$ nm/μs at the cantilever base position $Z = -100$ nm with data acquisition step of (a) 0.1 ns and (b) 10 ns.

It is a bit surprising that the ring-down oscillations have not been reported in the majority of nanofriction experimental papers, with the exception of [Fel16] and possibly very few others. It can be assumed that this has to do with the finite size of data acquisition frequency, which typically has the value of about 20 MHz [Gne09], i.e. force data are written into a file every 50 ns. To illustrate this point, we plot in Figure 4.2 the lateral

force for the same parameters as in Figure 4.1, but for $T = 300$ K and for the data acquisition time step of 0.1 ns (a) and 10 ns (b). It is seen in Figure 4.2(a) that the force oscillates in the stick phases even more than at zero temperature (cf. Figure 4.1(a) and Figure 4.2(a)), but if the data acquisition step is increased to the more experimentally relevant value of 10 ns, these oscillations look like random deviations and can be easily interpreted as resulting from thermal and instrumental noise.

4.2.2 Velocity dependence of friction

Shown in Figure 4.3 is the velocity-dependent friction force at different values of the distance Z from the cantilever base to the substrate. At low pulling velocities, the friction force increases logarithmically with V_{pull}, then it exhibits a maximum at $V_{max} = 0.025$ nm/μs, after which it sharply decreases and starts to increase again.

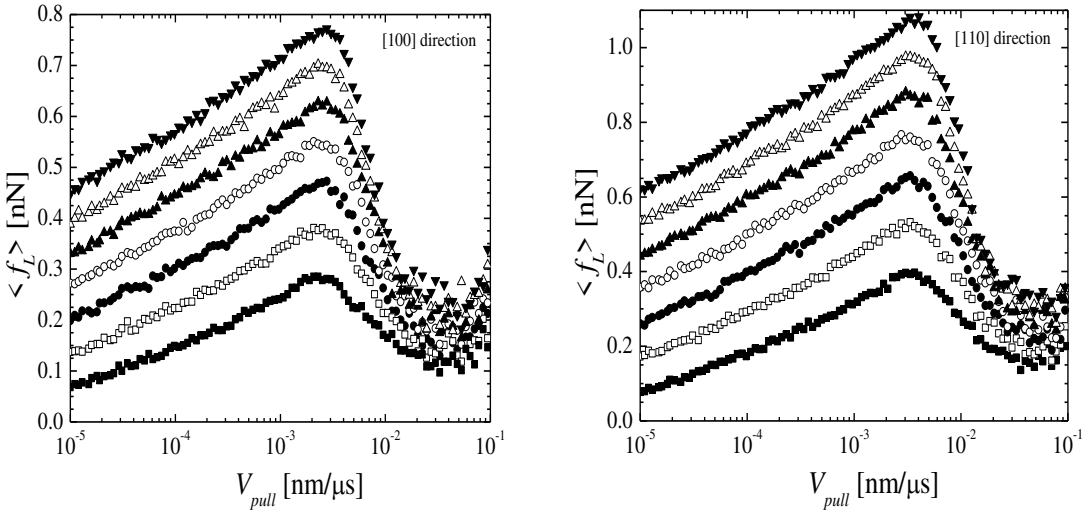

Figure 4.3: Average friction force vs. pulling velocity at $Z = 0$, -50, -100, -150, -200, -250, and -300 nm (from bottom to top). The normal load is approximately given by $-\kappa_N(Z + \sigma)$ with $\kappa_N = 0.1$ nN/nm and $\sigma = 0.3$ nm. Pulling proceeds along the x-axis, or [100] direction (left) and [110] direction (right).

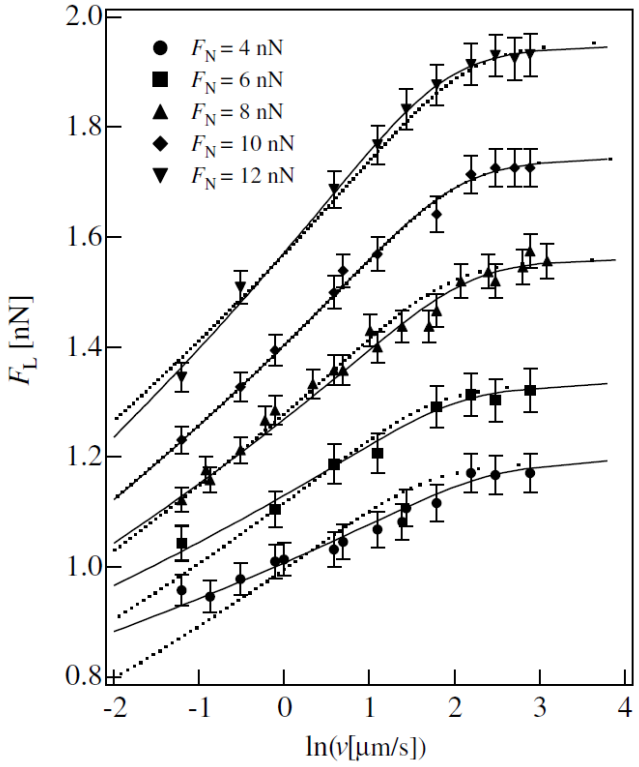

Figure 4.4: Average friction force vs. pulling velocity from [Rie03].

The logarithmic increase of friction is consistent with the experimental observations and simulations [San01, Rie03]. It arises due to the fact that the average number of slip events per unit time is proportional to the Arrhenius factor $e^{-\Delta U/kT}$, where ΔU is the (free) energy barrier height that separates the tip from the current minimum of the combined potential to the next. In the lowest order, this barrier height is related to the elastic force in the cantilever spring as $\Delta U \propto -f$. On the one hand, the average velocity of the cantilever must be the same as the pulling velocity; on the other hand, it must be proportional to the average number of slips per unit time. This implies that $V \propto e^{-\Delta U/kT}$; hence, $\Delta U \propto -kT \ln V$. But because $\Delta U \propto -f$, we conclude that the average friction force must increase logarithmically with pulling velocity.

The cantilever can be viewed as a harmonic oscillator periodically driven by the substrate potential. The periodicity of this driving is just the time to travel one lattice constant. When this time becomes comparable to the ring-down time discussed above, this excitation becomes resonant, and the cantilever starts to perform large-amplitude oscillations around the equilibrium value X. Hence, we can expect that the friction force should be minimal if the resonant condition

$$V = a\nu_{ringdown} \tag{4.4}$$

is fulfilled. With $a = 0.3$ nm and $\nu_{ringdown} = 0.133$ μs^{-1}, this gives the friction minimum at the velocity $V = 0.04$ nm/μs, in perfect agreement with the numerical results.

When the pulling velocity becomes even faster, corrugation of the substrate potential becomes irrelevant, and the friction force starts to decrease with velocity. For very fast pulling, the friction is due to the "viscous drag" of the substrate with the friction force increasing linearly with velocity as $\eta_S V$.

We are not aware of the experimental works reporting friction minimum at fast pulling. The closest experimental paper is [Rie03]. For comparison, we reproduce Figure 4.1 from [Rie03] here, see Figure 4.4 This work reports a friction plateau at V = 10 μm/s = 0.01 nm/μs. According to our calculations, this "plateau" is actually the summit of the friction peak, after which $\langle f_L \rangle$ should start to decrease. As seen in Figure 4.2, the position of this peak is found at about $V = 0.004$ nm/μs, in reasonable agreement with the value of 0.01 nm/ms from [Rie03]. This agreement indicates that the parameter values of our model are well-chosen.

4.3 Friction reduction by cantilever actuation

4.3.1 Including cantilever actuation into the model

In this section, we consider the effect of cantilever base vibrations on the friction force. By this, we mean that the cantilever base position is given by a time-dependent vector

$$\vec{R}(t) = \vec{R}_0 + \vec{V}t + \vec{n}_{osc}A\sin(\omega t). \quad (4.5)$$

By default, the initial position is $\vec{R}_0 = (0,0,Z_0)$,

where the parameter Z_0 determines the normal force according to Eq. (2.3). The pulling velocity has zero z-component. By default, we will consider only pulling along the x-axis, or [100] crystallographic direction, i.e.

$\vec{V} = (V,0,0)$.

The parameters A and ω denote oscillation amplitude and frequency, respectively. Finally, the unit vector $\vec{n}_{osc}$ specifies the direction of actuation. We will consider three cases:

Normal actuation: $\vec{n}_{osc} = \vec{e}_z$;

Lateral actuation: $\vec{n}_{osc} = \frac{\vec{V}}{V}$;

Transverse actuation: $\vec{n}_{osc} = \vec{e}_z \times \frac{\vec{V}}{V}$.

Here, $\vec{e}_z$ is a unit vector in the z-direction. Normal and lateral actuation have been considered in the literature both theoretically and experimentally, whereas the transverse actuation in the direction perpendicular to the pulling velocity and the z-axis seem to have been overlooked by the researchers in the field.

Presented in the rest of this section are the results for the following default parameters: $V = 10^{-4}$ nm/μs and $Z_0 = -100$ nm, for all actuation directions. This value of the normal coordinate corresponds to the normal load of about 10 nN.

4.3.2 Transverse actuation

As surprising as it may sound, transverse actuation has no effect on the average friction force and very little observable effect on the stick-slip curves. The average friction force remains the same for all driving amplitudes (A = 0…10 nm) and frequencies (ω =

0.001…10 μs^{-1}) tested. For the parameters chosen, this value is 0.448 nN at $T = 0$ and 0.3 nN at $T = 300$ K. Apparently, the transverse and the lateral coordinates of the cantilever tip are coupled to each other much less than the normal and the lateral ones.

4.3.3 Normal actuation

Figure 4.5 shows the average friction force vs. actuation frequency plot for normal actuation with the amplitude of (a) 10 nm and (b) 100 nm. Friction reduction at the lower actuation amplitude, panel (a), is relatively small, amounting to less than 10% of the friction force in the absence of actuation. The reason is just the small value of the normal cantilever stiffness used, see Section 4.1.2. At a smaller driving amplitude $A = 10$ nm, panel (a), only one friction minimum is observed at 0.52 μs^{-1} at $T = 0$. This peak shifts to 0.75 μs^{-1} at $T = 300$ K.

The normal resonance frequency of the cantilever, $\omega_N = \sqrt{\kappa_N/m_N}$ = 0.13 μs^{-1} is way too small to explain that peak. However, a better match is with the lateral frequency, $\omega_L = \sqrt{\kappa_L/m_L}$ = 0.58 μs^{-1}, which is very close to the resonant frequency observed at $T = 0$ for small-amplitude driving, see the upper curve in panel (a). Based on this agreement, it can be suggested that normal actuation may result in a reduction of friction by means of affecting the lateral motion of the cantilever. The coupling between the normal and lateral cantilever coordinates is possible, because of the second term, $U_1(z)\psi(x,y)$, in the potential (2.24). This suggestion does not explain the shifting of this peak to higher frequencies as the temperature increases; see the red curve in panel (a). Note that the friction minimum at $T = 300$ K is more symmetric than at 0 K.

At a larger driving amplitude $A = 100$ nm, the structure of the friction vs. frequency curve becomes more complex, as seen in panel (b). The curve now has several friction minima, which at $T = 0$ happen to be at 0.14, 0.23, 0.36, and 0.75 μs^{-1}. Increasing the temperature does not affect the location of these minima much, but the lower-frequency minima become suppressed.

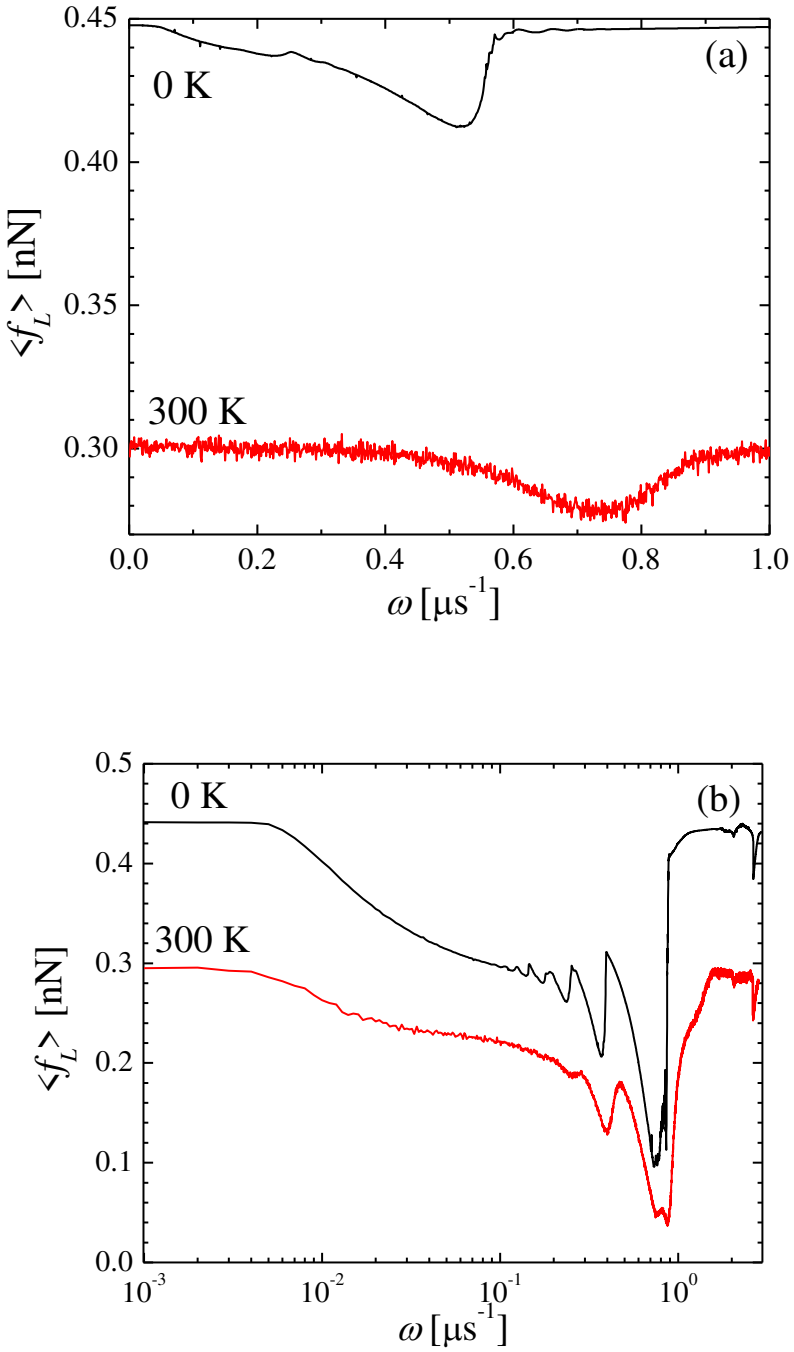

Figure 4.5: Average friction force vs. driving frequency for normal actuation with the amplitude (a) A = 10 nm and (b) A = 100 nm. In both panels, the upper black curve corresponds to T = 0, and the lower red curve corresponds to T = 300 K.

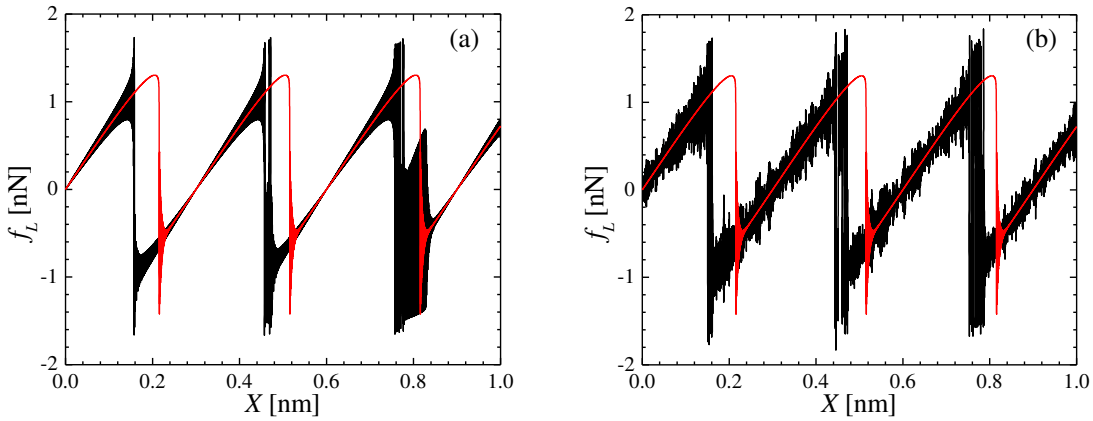

Figure 4.6: Lateral force vs. cantilever base position for normal actuation with the amplitude A = 100 nm and frequency ω = 0.75 μs^{-1}. Panel (a) T = 0; (b) T = 300 K. In both panels, the red curve is the lateral force at zero temperature in the absence of cantilever actuation.

Even at the driving frequency close to the global minimum, ω = 0.75 μs^{-1}, the motion of the cantilever proceeds in a stick-slip fashion, see Figure 4.6 showing the stick-slip curves at (a) T = 0 and (b) T = 300 K. For comparison, the stick-slip curves obtained at T = 0 at no actuation are shown in the same figure in red. Focusing on the T = 0 case, in the stick phases, the cantilever performs driven oscillations around the local potential minimum, and the amplitude of those oscillations increases as the cantilever base keeps moving. This results in a slip event occurring earlier than in the no-driving case, cf. the black and the red curves in Figure 4.6(a). Interestingly, even in the absence of thermal noise, the stick-slip curve is not regular, i.e. it is not the same in all stick phases. Some slip events are immediately followed by a back-slip, and some are followed by high-amplitude oscillations in the next stick phase. When the thermal noise is turned on, Figure 4.6(b), these irregularities become overshadowed by the thermal fluctuations of the cantilever.

4.3.4 Lateral actuation

The lateral actuation of the cantilever is a much better means of friction control. Already at the actuation amplitude of 0.01 nm the friction minimum is very pronounced, see Figure 4.7(a). The location of this global minimum at $\omega = 0.7$ μs^{-1} at $T = 0$ K and 0.8 μs^{-1} at $T = 300$ K roughly matches the lateral resonance frequency of the cantilever. Increasing the amplitude to 0.1 nm, Figure 4.7(b), results in the appearance of a complex multi peak structure of the friction vs. frequency curve, and this structure becomes less pronounced as the temperature is increased from 0K to 300 K.

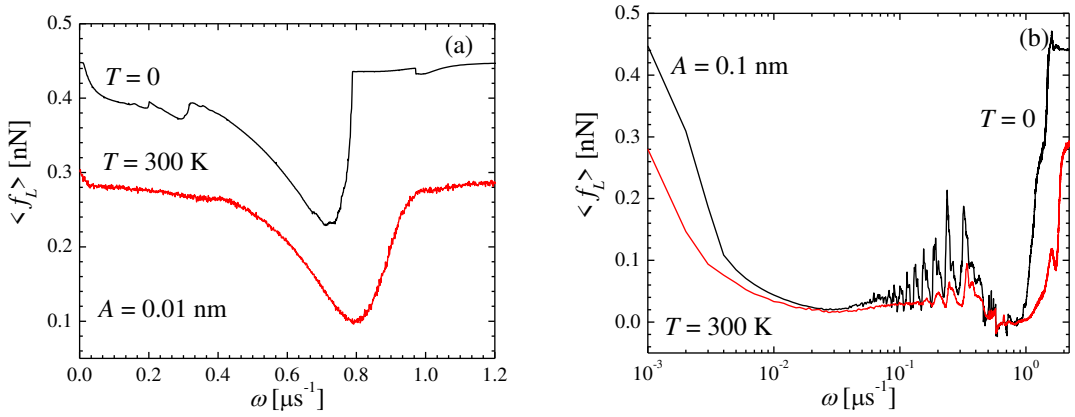

Figure 4.7: Average friction force vs. driving frequency for lateral actuation with the amplitude (a) $A = 0.01$ nm and (b) $A = 0.1$ nm. In both panels, the upper black curve corresponds to $T = 0$, and the lower red curve corresponds to $T = 300$ K.

Note that the plots in Figure 4.7 are roughly the same as in Figure 4.5, allowing us to conclude that normal and lateral actuation have a similar effect on the friction force. Because friction force is associated with the lateral deformation of the cantilever, the effect of the lateral actuation is much better pronounced than the effect of the normal actuation.

The friction vs. cantilever base position stick-slip curves for the driving amplitude $A = 0.01$ nm are shown in Figure 4.8. It is seen that at zero temperature, lateral actuation induces slip events earlier than in the undriven case (compare the red and the black curves

in Figure 4.8. At zero temperature, Figure 4.8 (a), the amplitude of the driven force oscillations increases at the end of each stick phase. This indicates that as the cantilever base moves relative to the substrate, the natural lateral frequency of the cantilever changes, becoming closer and closer to the actuation frequency. At some point, the tip oscillation amplitude becomes large enough to be able to overcome the barrier separating the tip from the next lattice site, resulting in a slip even happening earlier than without driving. When thermal noise is "turned on", it cooperates with this resonant slip effect in such a way that the slip happens even earlier than without noise. Also, thermal noise acting together with actuation makes it possible for the tip to jump back into the previous lattice site, as can be seen in Figure 4.8(b).

Presented in Figure 4.9 are the friction curves at absolute zero temperature for lateral driving amplitude of 0.1 nm and several frequencies from 0.001 to 2 μs^{-1}. At the lowest driving frequency $\omega = 0.001$ μs^{-1}, the tip performs the stick-slip motion modulated by the external forcing. The character of this modulation is somewhat unexpected, see Figure 4.9(a). The next lowest frequency from Figure 4.9(b), $\omega = 0.03$ μs^{-1}, corresponds to the broad friction minimum in Figure 4.7(b). It is seen in Figure 4.9(b) that in each stick phase, the tip performs driven oscillations with periodicity $\Delta X = 2\pi V/\omega = 0.021$ nm, and those oscillations are superimposed on the usual stick-slip curve. After a slip, the tip energy is not dissipated instantaneously, however. Rather, the tip moves a bit further than the next lattice site, thereby accumulating enough elastic energy to oscillate back into the previous lattice site. In this way, it performs several back-and-forth driven oscillations until it settles down in the next lattice site, so that a new stick phase begins.

At a higher driving frequency $\omega = 0.22$ μs^{-1}, Figure 4.9(c), the number of those large-amplitude oscillations increases, and the whole process becomes quite irregular. This irregularity is a bit surprising, given that the calculations were performed in the absence of thermal noise.

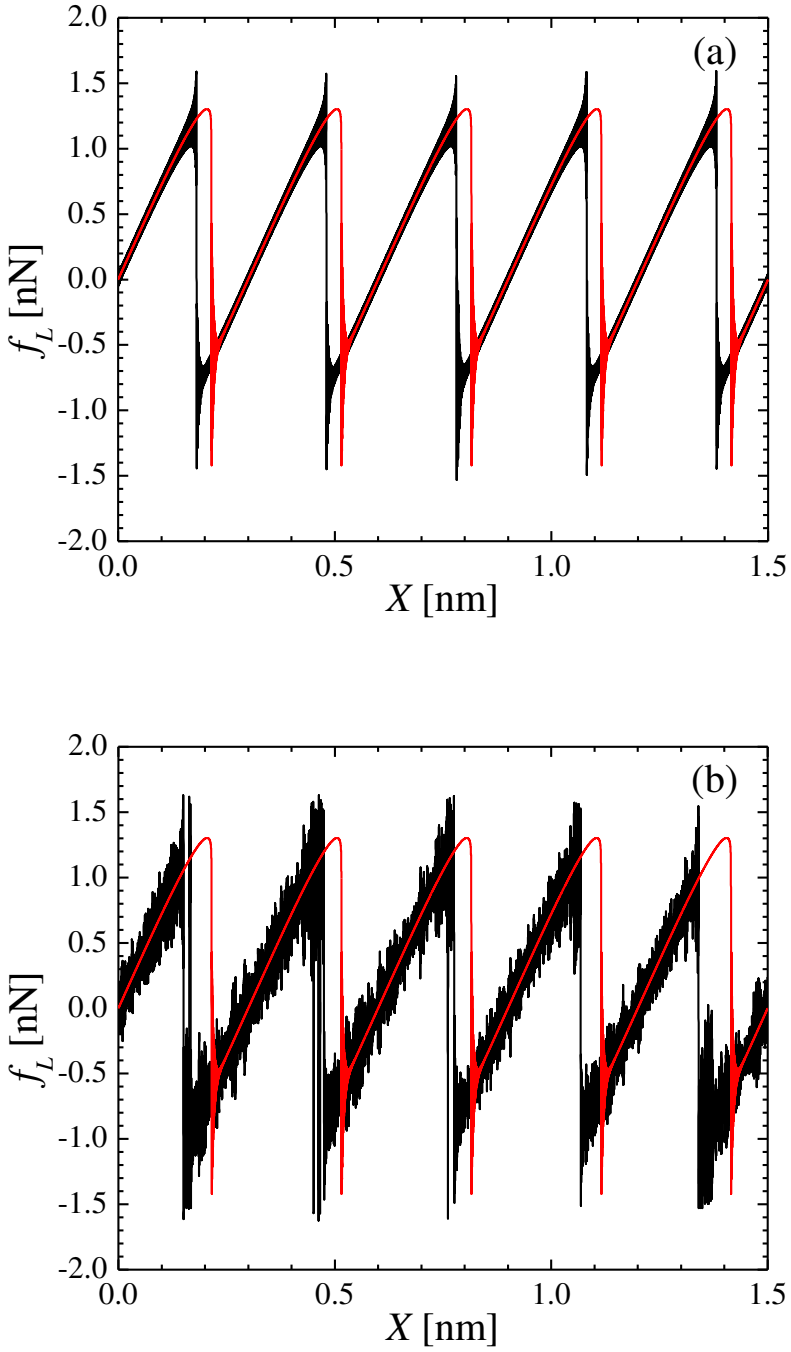

Figure 4.8: Stick-slip curve for the actuation amplitude $A = 0.01$ nm at (a) $T = 0$ K, $\omega = 0.7$ μs^{-1} and (b) $T = 300$ K, $\omega = 0.8$ μs^{-1}. In both panels, the red curve corresponds to the lateral force at zero temperature in the absence of actuation.

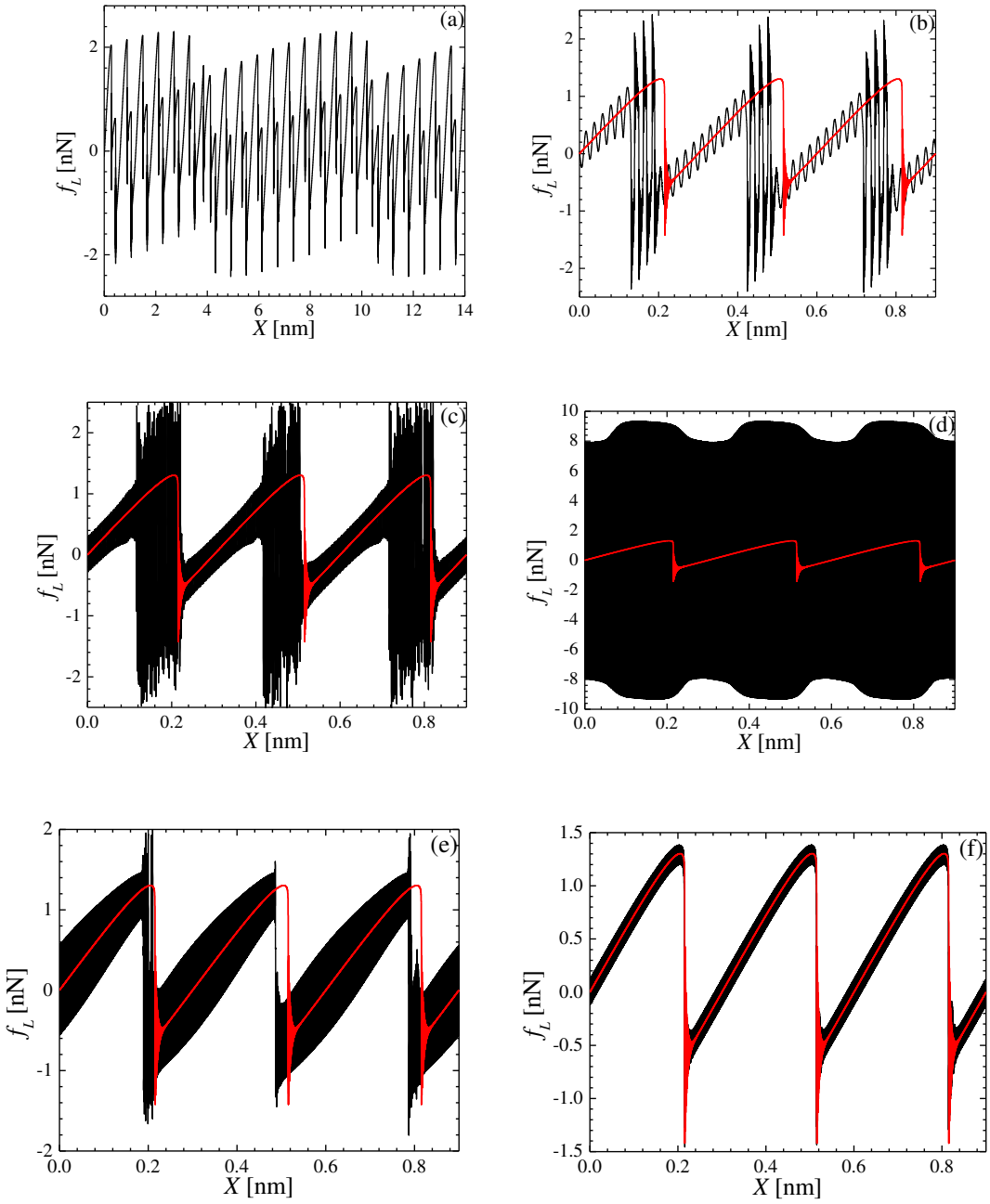

Figure 4.9: Friction force vs. cantilever base position at $T = 0$ for lateral driving amplitude A = 0.1 nm at the frequencies ω of (a) 0.001, (b) 0.03, (c) 0.2, (d) 0.6, (e) 1.3, (f) 2 μs^{-1}. The red curves correspond to the lateral force at zero temperature in the absence of actuation.

Further increase of the driving frequency to $\omega = 0.5\ \mu s^{-1}$ and $0.6\ \mu s^{-1}$ leads to a complete disappearance of the stick phases, see Figures 4.9(d). Rather, the cantilever performs large-amplitude driven oscillations around $x = X$. Those oscillations are modulated with the lattice periodicity of 0.3 nm.

Increasing the frequency results in the recovery of the stick-slip regime, because the cantilever's own response time is now too slow to follow the fast temporal variations of the external driving. Hence, it can be expected that the friction force will be performing very fast oscillations around the respective undriven curve. This is indeed what happens, see Figure 4.9(e) and (f). Note that the stick-slip curve at the smaller actuation frequency of $1.3\ \mu s^{-1}$ is somewhat irregular, but the regularity is recovered as ω is increased to 2 μs^{1}.

The behaviour of the friction force as a function of the actuation amplitude is complicated, see Figure 10 showing the simulation results for (a) $\omega = 10^{-3}\ \mu s^{-1}$ and (b) $\omega = 0.2\ \mu s^{-1}$ at $T = 0$ (black curve) and 300 K (red curve). At the smaller driving frequency, friction force monotonically decreases with the amplitude. This behaviour completely changes when the frequency increases to the value at which many minima and maxima start to be observed in Figure 4.7(b). At zero temperature, the friction force vs. amplitude curve is non-monotonically decreasing and consists of multiple irregular peaks initially (see the main plot). At higher amplitude, those peaks become much smaller in height, but they do not quite vanish (see inset). Interestingly, lateral oscillations of sufficiently high amplitude may result in the negative friction force, see inset.

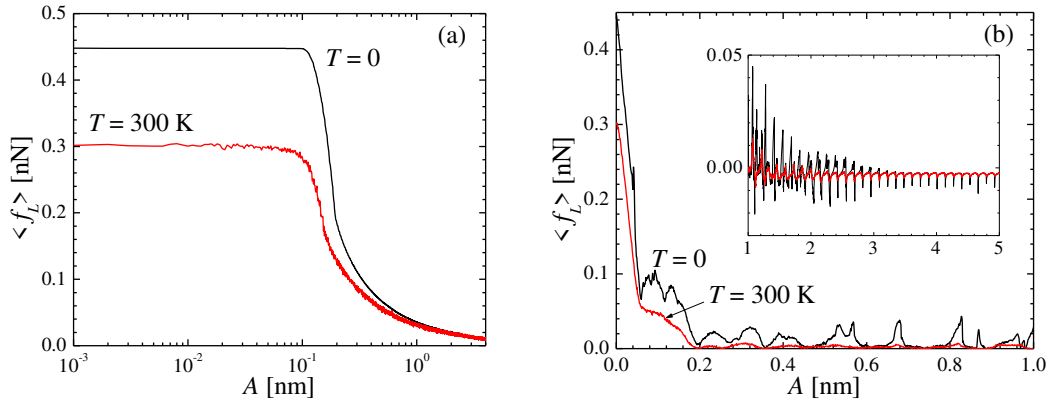

Figure 4.10: Friction force vs. driving amplitude at the driving frequency (a) ω = 0.001 μs^{-1} and (b) ω = 0.2 μs^{-1} at T = 0 (black curve) and 300 K (red curve). In panel (b), the main plot covers the range of A from 0 to 1 nm, and the inset covers the range of A between 1 and 5 nm.

We note that such a multipeaked structure has not been observed experimentally. Rather, experiment shows monotonic decrease of the friction force with lateral actuation amplitude [Rot14], similar to Figure 4.10(a). But the experimental measurements such as [Rot14], are usually performed at room temperature. On the other hand, as seen in Figure 10, the multipeaked structure becomes supressed as the temperature is elevated to 300 K. Therefore, it is a prediction of our model that decreasing the temperature should result in an onset of many maxima in the friction vs. driving amplitude curve.

Chapter V

Conclusions and outlook

5.1 Conclusions

In the course of this project, we considered a three-dimensional extension of the Prandtl-Tomlinson model of single-asperity nanoscale friction. Our model includes periodic modulation of the surface potential and damping coefficient, as well as the thermal noise effect due to the atomic degrees of freedom. It has been inspired by the model from [Wie11], but is more general than that model in that it includes cantilever damping coefficient and treats the substrate damping coefficient as position-dependent. An algorithm for numerical integration of the ensuing equations of motion is derived and shown to be optimal for the problems with position-dependent damping coefficient. Application of this algorithm to the 3dPT model has revealed the following features.

The motion of the tip in contact with a periodic crystalline surface proceeds in a stick-slip manner. Inertia plays an important role in the dynamics of an AFM cantilever in nanofriction experiments. Its role is manifested in the ring-down effect, i.e. regular damped oscillations of the lateral force after each slip event. However, in the experiment, these ring-down oscillations are rarely detected, because the frequency of data collection is usually much smaller than the frequency of those oscillations. Furthermore, when the mean friction force is measured as a function of the pulling velocity, it initially increases logarithmically, then develops a maximum, and then sharply drops to a minimum. The friction minimum occurs at such pulling velocity that the inverse time to cover one lattice constant matches almost exactly the ring-down frequency.

A further effect of the cantilever inertia is the possibility to control friction forces by means of periodic actuation of the cantilever. This actuation may proceed in the normal or lateral direction, whereas transverse actuation of the cantilever has no detectable effect on the average friction force. Normal motion of the cantilever base can affect its lateral coordinate, whereas the transverse motion cannot.

The effect of actuation on the friction force is more apparent at zero temperature than at room temperature. As a function of actuation frequency, the friction force exhibits multiple minima both for normal and lateral actuation. Those minima are more pronounced at the higher actuation amplitude and at the lower temperature. Likewise, when measured as a function of the actuation amplitude at fixed frequency, the friction force exhibits many irregular maxima at zero temperature; those maxima get supressed when the temperature is increased to 300 K.

Many different dynamic regimes of the cantilever motion can be realized depending on the actuation parameters. When thermal noise is present, the difference between those regimes becomes less sharp than in the noise-free limit.

5.2 Future work

The results obtained in this thesis demonstrate a richness of dynamic regimes in an apparently simple 3dPT model of nanoscale friction with external actuation. However, the 3dPT model used in this thesis is oversimplified in two respects discussed below.

Cantilever apex elasticity. There is plenty of experimental evidence that the cantilever apex cannot be treated as a rigid body, as done in our model. For example, the slope of the stick-slip curve in each stick phase, df/dX, see Fig. 4.2(a), is only slightly smaller than the lateral spring constant value of 10 N/m used in our calculations. The experimental stick-slip curves, however, exhibit a much smaller slope in the range between 1 and 5 N/m [Sch06, Evs06, Jan10]. This can only be explained by the fact that the cantilever apex is a soft object with elasticity κ_{apex} = 1…5 N/m in this range. Then, because the cantilever beam and the tip apex represent two springs connected in series, and taking into account the elastic deformation of the substrate, the net elasticity measured as the slope of the stick-slip curve is given by $1/(\kappa_L^{-1} + \kappa_{apex}^{-1} + \kappa_{substrate}^{-1})$. It is smaller that both κ_L and κ_{apex}.

In principle, there is no problem to take the elasticity of the tip apex into account by introducing additional degrees of freedom describing the deformation of the apex. In the simplest extension, this deformation could be just a single number, e.g. the deformation angle. Unfortunately this would severely slow down the calculations, because the tip apex is so light that its oscillation period is in the nanosecond range [Kry06, Kry07]. This means that the time step would have to be of the order of 50 ps or smaller, as opposed to 50 ns value used in our simulations. In other words, simulation time would be increased by at least a factor of 1000. Given that the computation time to generate a plot such as the one from Fig. 4.3 or 4.5 was of the order of several hours, this calculation with the apex elasticity would take weeks or even months.

Contact aging. It has recently been established experimentally that the tip-substrate contact strengthens itself in the course of time [Evs06, Evs08, Evs13(a), Maz17]. The

origin of contact aging is not firmly established. Under the ambient conditions, this could be formation of capillary water bridges; in the experiments done in the ultra-high vacuum, contact aging must proceed via some other mechanism. The nature of that mechanism can only be hypothesized at present. But taking into account contact aging effect at a phenomenological level is possible by introducing additional internal variables into the model that would describe the state of the tip-substrate contact [Maz17].

Proper incorporation of the apex elasticity and contact aging effects are important extensions of the simple 3dPT model investigated in this thesis.

References

[All91] M. Allen and D. Tildesley. *Computer Simulations of Liquids.* Oxford Univeristy Press, Oxford (1991).

[Arc57] J.F. Archard. *Elastic Deformation and the Laws of Friction.* Rroc. R. Soc. A **243**, 190 (1957).

[Arg96] C. Argento and R.H. French. *Parametric tip model and force–distance relation for Hamaker constant determination from atomic force microscopy.* J. Appl. Phys. **80**, 6081 (1996).

[Ben99] R. Bennewitz, T. Gyalog, M. Guggisberg, M. Bammerlin, E. Meyer, and H.-J. Güntherodt. *Atomic-scale stick-slip processes on Cu(111).* Phys. Rev. B **60**, R11301 (1999).

[Bin86] G. Binnig, C.F. Quate, and Ch. Gerber. *Atomic Force Microscope.* Phys. Rev. Lett **85** 302 (1986).

[Bow01] F. P. Bowden and D. Tabor. *The Friction and Lubrication of Solids.* Oxford University Press, Oxford (2001).

[Car97] R.W. Carpick, D.F. Ogletree, and M. Salmeron. *Lateral stiffness: A new nanomechanical measurement for the determination of shear strengths with friction force microscopy.* Appl. Phys. Lett. **70**, 1548 (1997).

[Col96] J. Colchero, A.M. Baró, and O. Marti. *Energy dissipation in scanning force microscopy friction on an atomic scale.* Trib. Lett. **2**, 327 (1996).

[Erm78] D. L. Ermak and J.A. McCammon. *Brownian Dynamics with Hydrodynamic Interactions*. J. Chem. Phys. **69**, 1352 (1978).

[Erm80] D. L. Ermak and H. Buckholtz. *Numerical Integration of the Langevin Equation: Monte Carlo Simulation.* J. Comput. Phys. **35**, 169 (1980).

[Evs06] M. Evstigneev, A. Schirmeisen, L. Jansen, H. Fuchs, and P. Reimann. *Force Dependence of Transition Rates in Atomic Friction*. Phys. Rev. Lett. **97**, 240601 (2006).

[Evs08] M. Evstigneev, A. Schirmeisen, L. Jansen, H. Fuchs, and P. Reimann. *Contact ageing in atomic friction.* J. Phys.: Condens. Matter **20**, 254001 (2008).

[Evs10] M. Evstigneev and P. Reimann. *Langevin equation for a system nonlinearly coupled to a heat bath.* Phys. Rev. B **82**, 224303 (2010).

[Evs13] M. Evstigneev and P. Reimann. *Stick-slip statistics in atomic friction*. Phys. Rev. B **87**, 205441 (2013).

[Evs13a] M. Evstigneev and P. Reimann. *Thermally Activated Contact Strengthening Explains Nonmonotonic Temperature and Velocity Dependence of Atomic Friction*. Phys. Rev. X **3**, 041020 (2013).

[Evs19] M. Evstigneev and A. Al-Haidari. *Brownian motion on a stochastic harmonic oscillator chain: limitations of the Langevin equation*. J. Phys. A: Math. Theor. **52**, 055001 (2019).

[Fel16] M. Feldmann, D. Dietzel, A. Tekiel, J. Topple, P. Grütter, and A. Schirmeisen. *Universal Aging Mechanism for Static and Sliding Friction of Metallic Nanoparticles.* Phys. Rev. Lett. **117**, 025502 (2016).

[Fre96] D. Frenken and B. Smit. *Understanding Molecular Simulation*. Academic Press, 1996.

[Gos11] N.N. Gosvami, M. Feldmann, J. Peguiron, M. Moseler, A. Schirmeisen, and R. Bennewitz. *Ageing of a Microscopic Sliding Gold Contact at Low Temperatures.* Phys. Rev. Lett. **107**, 144303 (2011)

[Gne09] E. Gnecco, A. Socoliuc, S. Maier, J. Gessler, T. Glatzel, A. Baratoff, and E. Meyer. *Dynamic superlubricity on insulating and conductive surfaces in ultra-high vacuum and ambient environment.* Nanotechnology **20**, 025501 (2009).

[Hol08] H. Hölscher, D. Ebeling, and U.D. Schwarz. *Friction at Atomic-Scale Surface Steps: Experiment and Theory.* Phys. Rev. Lett. **101**, 246105 (2008).

[Isr11] J. Israelachvili. *Intermolecular and Surface Forces.* 3rd Edition. Academic Press (2011).

[Jan10] L. Jansen, H. Hölscher, H. Fuchs, and A. Schirmeisen. *Temperature Dependence of Atomic-Scale Stick-Slip Friction*. Phys. Rev. Lett. **104**, 256101 (2010).

[Joh98] K.L. Johnson and J. Woodhouse. *Stick–slip motion in the atomic force microscope.* Trib. Lett. **5**, 155 (1998).

[Kri91] J. Krim, D.H. Solina, and R. Chiarello. *Nanotribology of a Kr Monolayer: A Quartz-Crystal Microbalance Study of Atomic-Scale Friction*. Phys. Rev. Lett. **66**, 181 (1991).

[Kri13] J. Krim. *Friction at the nanoscale.* In: Q.J. Wang Q.J. and Y.W. Chung (eds.), *Encyclopedia of Tribology*. Springer, Boston, MA (2013).

[Kry06] S.Yu. Krylov, J.A. Dijksman, W.A. van Loo, and J.W.M. Frenken. *Stick-Slip Motion in Spite of a Slippery Contact: Do We Get What We See in Atomic Friction?* Phys. Rev. Lett. **97**, 166103 (2006).

[Kry07] Krylov, S.Y., Frenken, J.W.M. *Thermal Contact Delocalization In Atomic Scale Friction: A Multitude Of Friction Regimes.* New J. Phys. 9 (2007) 398.

[Kry14] Yu. Krylov and W. Frenken, *The Physics of Atomic-Scale Friction: Basic Considerations and Open Questions.* Phys. Status Solidi B **251**, 711 (2014).

[Kub66] R. Kubo. *The fluctuation-dissipation theorem*. Rep. Progr. Phys. **29**, 255 (1966).

[Lan97a] M.A. Lantz, S.J. O'Shea, M.E. Welland, and K.L. Johnson. *Atomic-force-microscope study of contact area and friction on $NbSe_2$*. Phys. Rev. B **55**, 10 776 (1997).

[Lan97b] M.A. Lantz, S.J. O'Shea, A.C.F. Hoole, and M.E. Welland. *Lateral stiffness of the tip and tip-sample contact in frictional force microscopy.* Appl. Phys. Lett. **70**, 970 (1997).

[Lan10] G. Langewisch, H. Fuchs and A. Schirmeisen. *Temperature dependence of energy dissipation on NaCl(001) in non-contact atomic force microscopy*. Nanotech. **21** 345703 (2010).

[Mai05] S. Maier, Yi Sang, T. Filleter, M. Grant, R. Bennewitz, E. Gnecco and E. Meyer. *Fluctuations and jump dynamics in atomic friction experiments.* Phys. Rev. B **72**, 245418 (2005).

[Mat87] C.M. Mate, G.M. McClelland, R. Erlandsson, and S. Chiang. *Atomic-Scale Friction of a Tungsten Tip on a Graphite Surface*. Phys. Rev. Lett. **59**, 1942 (1987).

[Maz17] J.J. Mazo, D. Dietzel, A. Schirmeisen, J.G. Vilhena, and E. Gnecco. *Time Strengthening of Crystal Nanocontacts.* Phys. Rev. Lett. **118**, 246101 (2017).

[Med06] S.N. Medyanik, W.K. Liu, I.-H. Sung, and R. W. Carpick. *Predictions and Observations of Multiple Slip Modes in Atomic-Scale Friction*. Phys. Rev. Lett. **97**, 136106 (2006).

[Mer15] F.Mertens, T. Göddenhenrich, V. Lushta, and A. Schirmeisen. *Dynamic friction-force microscopy using fractional-resonance excitation: Image contrast of graphite surface defects*. Phys. Rev. B **91**, 235414 (2015).

[Nak05] J. Nakamura, S. Wakunami, and A. Natori. Double-slip mechanism in atomic-scale friction: Tomlinson model at finite temperatures. Phys. Rev. B **72**, 235415 (2005).

[Pit14] A.A. Pitenis, D. Dowson, and W. G. Sawyer. *Leonardo da Vinci's Friction Experiments: An Old Story Acknowledged And Repeated.* Tribol. Lett. **56**, 509 (2014).

[Pra28] L. Prandtl. *Ein Gedankenmodell zur kinetischen Theorie der festen Körper*, Z. Angew. Math. Mech. **8**, 85–106 (1928). See English translation by

[Pre99] W.H. Press, S.A. Teukolsky, W.T. Vetterlilng, and B.P. Flannery. *Numerical Recipes in C*. Cambridge Univ. Press, 1999.

[Pop12] V.L. Popov and J.A.T. Gray. Prandtl-Tomlinson model: History and applications in friction, plasticity, and nanotechnologies. Z. Angew. Math. Mech. **92**, 683 (2012).

[Rie03] E. Riedo, E. Gnecco, R. Bennewitz, E. Meyer, and H. Brune. *Interaction Potential and Hopping Dynamics Governing Sliding Friction.* Phys. Rev. Lett. **91**, 084502 (2003).

[Rei04] P. Reimann and M. Evstigneev. *NonmonotonicVelocity Dependence of Atomic Friction*. Phys. Rev. Lett. **93**, 230802 (2004).

[Rei05] P. Reimann and M. Evstigneev. *Description of atomic friction as forced Brownian motionn.* New J. Phys. **7**, 25 (2005).

[Ric03] A. Ricci and G. Ciccotti. *Algorithms for Brownian Dynamics.* Mol. Phys. **101**, 1927 (2003).

[Rie03] E. Riedo, E. Gnecco, R. Bennewitz, E. Meyer, and H. Brune. *Interaction Potential and Hopping Dynamics Governing Sliding Friction.* Phys. Rev. Lett. **91**, 084502 (2003).

[Rot10] R. Roth, T. Glatzel, P. Steiner, E. Gnecco, A. Baratoff, and E. Meyer. *Multiple Slips in Atomic-Scale Friction: An Indicator for the Lateral Contact Damping.* Tribol. Lett. **39**, 63 (2010).

[Rot14] R. Roth, O.Y. Fajardo, J.J. Mazo, E. Meyer, and E. Gnecco. *Lateral vibration effects in atomic-scale friction*. Appl. Phys. Lett. **104**, 083103 (2014).

[San01] Y. Sang, M. Dubé, and M. Grant. *Thermal Effects on Atomic Friction*. Phys. Rev. Lett. **87**, 174301 (2001).

[Sch05] A. Schirmeisen, L. Jansen, and H. Fuchs. *Tip-jump statistics of stick-slip friction.* Phys. Rev. B **71**, 245403 (2005).

[Sch06] A. Schirmeisen, L. Jansen, H. Hölscher, and H. Fuchs. *Temperature dependence of point contact friction on silicon.* Appl. Phys. Lett. **88**, 123108 (2006).

[Soc04] A. Socoliuc, R. Bennewitz, E. Gnecco and E. Meyer. *Transition from Stick-Slip to Continuous Sliding in Atomic Friction: Entering a New Regime of Ultralow Friction.* Phys. Rev. Lett. **92**, 134301 (2004).

[Soc06] A. Socoliuc, E. Gnecco, S. Maier, O. Pfeiffer, A. Baratoff, R. Bennewitz, and E. Meyer. *Atomic-Scale Control of Friction by Actuation of Nanometer-Sized Contacts.* Science **313**, 207 (2006).

[Ste09] P. Steiner, R. Roth, E. Gnecco, A. Baratoff, S. Maier, Th. Glatzel, and E. Meyer. *Two-dimensional simulation of superlubricity on NaCl and highly oriented pyrolytic graphite.* Phys. Rev. B **79**, 045414 (2009).

[Tab69] D. Tabor and R.H.S. Winterton. *The Direct Measurement of Normal and Retarded van der Waals Forces.* Proc. Royal Soc. A **312**, 435 (1969)

[Tia13] Y. Tian. *Surface Force Apparatus.* In: Q.J. Wang and Y.W. Chung (eds). *Encyclopedia of Tribology*. Springer, Boston, MA (2013).

[Tom29] G. A. Tomlinson, *A Molecular Theory of Friction*, Philos. Mag. **7**, 905 (1929).

[Tsh05] Z. Tshiprut, A.E. Filippov, and M. Urbakh. *Tuning Diffusion and Friction in Microscopic Contacts By Mechanical Excitations.* Phys. Rev. Lett. **95**, 016101 (2005).

[Tsh09] Z. Tshiprut, S. Zelner, and M. Urbakh. *Temperature-Induced Enhancement of Nanoscale Friction.* Phys. Rev. Lett. **102**, 136102 (2009)

[Wie11] C. Wieferink, P. Krüger, and J. Pollmann. *Simulations of friction force microscopy on KBr(001) surface based on ab initio calculated tip-sample forces*. Phys. Rev. B **83** 235328 (2011).

[Yuy11] P.A. Yuya, D. C. Hurley, and J.A. Turner. *Relationship between Q-factor and sample damping for contact resonance atomic force microscope measurement of viscoelastic properties.* J. Appl. Phys. **109**, 113528 (2011).